

Article

Use of Multiscale Data-Driven Surrogate Models for Flowsheet Simulation of an Industrial Zeolite Production Process

Vasyl Skorych ^{1,*}, Moritz Buchholz ^{1,†}, Maksym Dosta ^{1,2}, Helene Katharina Baust ³, Marco Gleiß ³, Johannes Haus ⁴, Dominik Weis ⁴, Simon Hammerich ⁴, Gregor Kiedorf ⁴, Norbert Asprion ⁴, Hermann Nirschl ³, Frank Kleine Jäger ⁴ and Stefan Heinrich ¹

¹ Institute of Solids Process Engineering and Particle Technology, Hamburg University of Technology, 21073 Hamburg, Germany

² Boehringer Ingelheim Pharma GmbH & Co., KG, 88400 Biberach an der Riss, Germany

³ Institute of Mechanical Process Engineering and Mechanics, Karlsruhe Institute of Technology, 76131 Karlsruhe, Germany

⁴ BASF SE, 67056 Ludwigshafen, Germany

* Correspondence: vasy.skorych@tuhh.de

† These authors contributed equally to this work.

Abstract: The production of catalysts such as zeolites is a complex multiscale and multi-step process. Various material properties, such as particle size or moisture content, as well as operating parameters—e.g., temperature or amount and composition of input material flows—significantly affect the outcome of each process step, and hence determine the properties of the final product. Therefore, the design and optimization of such processes is a complex task, which can be greatly facilitated with the help of numerical simulations. This contribution presents a modeling framework for the dynamic flowsheet simulation of a zeolite production sequence consisting of four stages: precipitation in a batch reactor; concentration and washing in a block of centrifuges; formation of droplets and drying in a spray dryer; and burning organic residues in a chain of rotary kilns. Various techniques and methods were used to develop the applied models. For the synthesis in the reactor, a multistage strategy was used, comprising discrete element method simulations, data-driven surrogate modeling, and population balance modeling. The concentration and washing stage consisted of several multicompartment decanter centrifuges alternating with water mixers. The drying is described by a co-current spray dryer model developed by applying a two-dimensional population balance approach. For the rotary kilns, a multi-compartment model was used, which describes the gas–solid reaction in the counter-current solids and gas flows.

Keywords: flowsheet simulation; zeolite production; data-driven modeling; synthesis; solid–liquid separation; spray drying; kiln; multiscale modeling



Citation: Skorych, V.; Buchholz, M.; Dosta, M.; Baust, H.K.; Gleiß, M.; Haus, J.; Weis, D.; Hammerich, S.; Kiedorf, G.; Asprion, N.; et al. Use of Multiscale Data-Driven Surrogate Models for Flowsheet Simulation of an Industrial Zeolite Production Process. *Processes* **2022**, *10*, 2140.

<https://doi.org/10.3390/pr10102140>

Academic Editors: Krzysztof Talaśka, Szymon Wojciechowski and Antoine Ferreira

Received: 26 August 2022

Accepted: 15 October 2022

Published: 20 October 2022

Publisher's Note: MDPI stays neutral with regard to jurisdictional claims in published maps and institutional affiliations.



Copyright: © 2022 by the authors. Licensee MDPI, Basel, Switzerland. This article is an open access article distributed under the terms and conditions of the Creative Commons Attribution (CC BY) license (<https://creativecommons.org/licenses/by/4.0/>).

1. Introduction

Zeolites have a wide range of applications, e.g., in the chemical industry as catalysts [1], adsorption material [2], or molecular sieves [3]. Due to the large specific surface area, the high thermal stability, and the possibility for the development of tailor-made pore systems, zeolites are especially suitable for these applications [4]. Zeolites have a mostly crystalline structure based on aluminosilicates resulting in an intrinsic acidity that act as catalytic sites for many reactions [5].

Because of such versatile properties, interest in zeolite materials is only growing. In particular, recent theoretical modeling of the processes associated with zeolites has greatly advanced the understanding of these materials. Nowadays, a wide variety of methods and approaches are used for their computer-aided simulations. However, most of them are focused on modeling the synthesis processes taking place in the reactor. Among the most commonly applied methods are molecular mechanics and molecular dynamics [6–9].

Atomic simulations were also used to investigate zeolite structure and stability [10–12]. To computationally predict structure of zeolites, as well as to study their absorption mechanisms and ion exchange, Monte Carlo methods were applied [13–16]. Many other techniques, like cluster modeling for describing zeolite reactivity [17], transition interface sampling simulations for the theoretical study of zeolite synthesis [18], or lattice energy minimization to obtain structural information on zeolites [19] were also actively used.

On larger scales, population balance methods (PBM) were applied for analyzing crystallization behavior [20], kinetics of nucleation and crystal growth [21], and prediction of the particle size distribution (PSD) of zeolites [22,23]. Additionally, coupling of PBM and discrete element method (DEM) was utilized for multiscale modeling of zeolite particles breakage [24].

The application of machine learning techniques has also expanded substantially in recent years [12]. For example, they were used for design and discovery of new zeolites [25], or for prediction the formation of energetically stable hypothetical zeolites [26].

At the same time, only a limited number of the macroscale simulations of the zeolite processing chain are available in the literature. For example, Farag and Zhang [27] used flowsheet simulation to evaluate energy efficiency of several manufacturing processes. Salam et al. [28] performed batch flowsheet simulation of a lab-scale process of zeolite synthesis from metakaolin, including dealumination, gel formation, crystallization, filtration and drying steps.

In this work, a common way of producing high-volume zeolite catalysts, which involves a hydrothermal synthesis step [29], followed by a solid–liquid separation and a subsequent drying stage is studied. Here, often spray drying is used due to the favorable and efficient particle formulation behavior. A final calcination step is applied to remove the remaining side products and receive the desired product properties.

For the production process of zeolites, both the operational parameters, like the process temperature and pressure, and the intermediate material properties, such as the particle size distribution and the moisture content, determine the performance of different process steps and therefore the final product properties. The design and optimization of such connected processes can be supported by simulative methods to allow for a holistic view of the whole process. Due to the high complexity of the single process steps, an application of flowsheet simulations is suitable to efficiently compute the transient behavior of the whole production process. However, flowsheet simulations rely on reduced-order models which capture only the main system behavior. To increase the accuracy of such simplified models, the information from resolved simulations can be incorporated. This offers the possibility to describe the most relevant process and product parameters over the whole production chain using the reduced-order models.

In this work, to develop models of all steps of the zeolite production process, various techniques are used. For the synthesis reactor, a novel approach to model the process on multiple scales is presented. Therefore, the particle growth and agglomeration behavior inside the synthesis reactor is described in detail by way of a discrete element method simulation, which models particle–particle interactions inside a representative control volume. By using artificial neural networks (ANN), the information on the particle dynamics is extracted and put into a condensed population balance model, which is used in the reduced-order model for the flowsheet simulation [30,31]. The solid–liquid separation stage is described by a multi-compartment centrifuge model, developed by Gleiss et al. [32–34], which considers sedimentation and compaction of the cake. The population balance approach for a co-current spray drying model, presented by Buchholz et al. [35], allows us to consider different drying kinetics and particle solidification inside the drying chamber. The information on the drop movement through the spray dryer is extracted from computational fluid dynamics (CFD) simulations to further increase the accuracy of the model [35]. The calcination of zeolites is performed within a rotary kiln. It is described by a multi-compartment model to reflect the gradients along the kiln axis. The model is based on the work of Küssel [36]. The information on particle movement and reaction

inside the solid bed are extracted from coupled CFD-DEM simulations. To account for the multi-dimensional nature of the zeolite properties, like the particle size distribution and moisture content, the open-source simulation framework Dyssol [37–39] is used. It enables a combination of all developed models into a single flowsheet and a simulation of the whole process. This software was specifically developed for dynamic flowsheet simulation of interconnected processes involving granular materials.

2. Model

The flowsheet of the considered zeolite catalyst production process with corresponding material components is shown in Figure 1. The catalyst particles (Ze) are formed due to agglomeration of precipitated reaction products within the synthesis unit operation. This unit is operated in batch mode. As the following processes are operated continuously, the synthesis step is calculated separately and its product is fed to the first centrifuge continuously. Between the two centrifugation stages, the slurry is washed with fresh water to remove hazardous byproducts from the concentrated slurry. The efficiency of the centrifuges depends strongly on the particle sizes of the zeolite products, which are in the range of nanometers. When the concentrated slurry enters the spray drying stage through a nozzle, the primary particles within the atomized suspension droplets agglomerate to larger particles in the micrometer range. Starting from the spray drying stage, the particle size grid is therefore adapted to larger product agglomerates. For the calcination, a rotary kiln with heated walls is used. In the first calcination stage, remaining water from the spray-dried particles evaporates. To avoid too high temperatures during the combustion of the organic residues, the first calcination stage is operated with a low oxygen concentration of the incoming gas. In the second calcination stage, the remaining organic residues are burned out of the product.

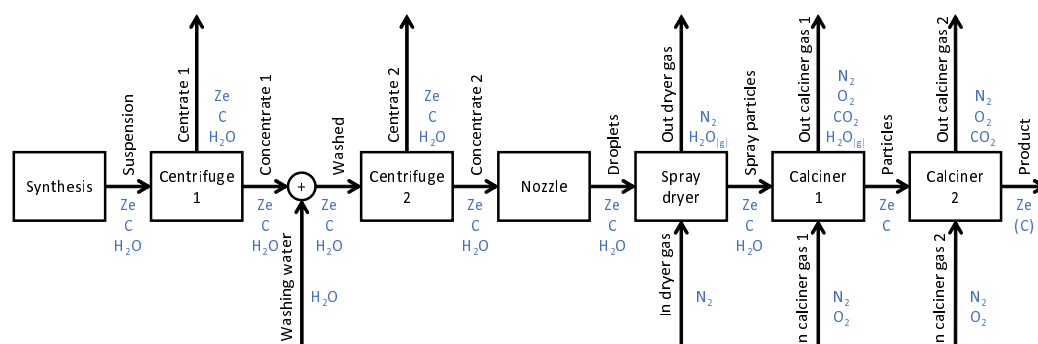


Figure 1. Flowsheet of a zeolite catalyst production process with the corresponding compositions of the material flows.

2.1. Synthesis

The zeolite synthesis process, taking place in the reactor, can be divided into several stages. In the beginning, the so-called unit cells are obtained from the initial reagents as a result of chemical transformations. These reactions can be mapped using fairly simple reaction kinetics. The emerged unit cells then precipitate, forming crystalline particles. An important final stage of the process is the agglomeration of the precipitated particles. This can be depicted using population balance models, parameterized with DEM simulations.

Since the real compounds, as well as some of their properties, cannot be disclosed for confidentiality reasons, the materials in the text are encrypted, and some of their parameters are changed.

2.1.1. General Model Structure

The influence of different process conditions on the synthesis is often difficult to predict since many parameters are interdependent. To facilitate this task, a multi-step

strategy to develop a macroscale synthesis model suitable for flowsheet simulations is suggested. The general scheme of this approach is shown in Figure 2. It comprises the following steps:

1. DEM is used to generate statistics on particle collisions for various values of process and material parameters;
2. Obtained information is used to find individual contributions of several empirical agglomeration kernels to the overall growth;
3. Found contributions and variations of process and material parameters are used to train a data-driven surrogate model of the agglomeration kernel;
4. The derived kernel is applied to build a PBM used in flowsheet simulations.

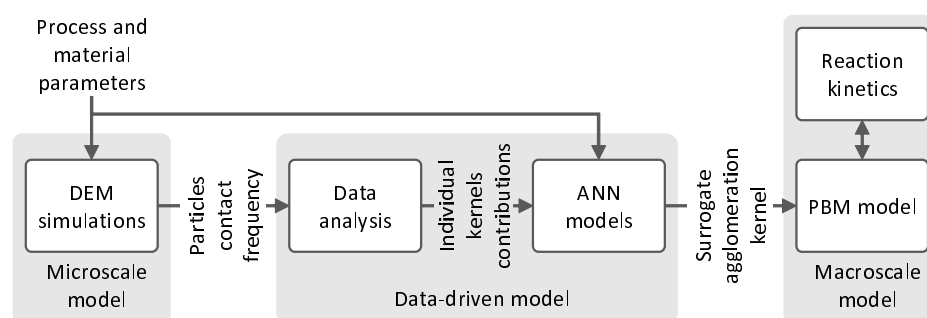


Figure 2. General scheme of the approach to develop a macroscale synthesis model.

2.1.2. Microscale Model

DEM simulations with a variation of four process parameters were performed to extract statistics about the particles contact frequencies, needed to determine the agglomeration kernel. These are listed together with their limits in Table 1. Latin hypercube sampling was utilized to generate a near-random set of parameter values in this 4-dimensional distribution. In total, 1200 samples with different combinations of parameters have been generated and simulated.

Table 1. Input process and material parameters for DEM simulations.

Parameter		Min	Max	Units
Temperature	T	400	485	K
Viscosity	η	0.0008	0.0024	Ns m^{-2}
Shear rate	$\dot{\Gamma}$	6	300	s^{-1}
Surface energy	γ	0.03	0.3	J m^{-2}

The Johnson–Kendall–Roberts (JKR) model [40] was used to describe cohesive forces in particle–particle collisions. The corresponding equations are given in Appendix A.1.1. To simulate the Brownian- and shear-induced particle motion in the liquid phase, the diffusion model of Depta et al. [41] was adapted. Along with the temperature-dependent Brownian motion of particles, it allows defining a velocity profile for particles depending on their coordinates along the vertical axis (Z), thus enabling the simulation of particles shear. The model is described in Appendix A.1.2.

To generate the initial scene, 50,000 particles were placed in a cubic volume with a side length of 43.211 μm , using an iterative force-biased algorithm [42]. The generation volume was limited by periodic boundary conditions (PBC) on all sides, which made it possible to use such a small number of simulated objects (and, hence, to have acceptable simulation times), while maintaining the quantity and quality of obtained statistics. Given this number of particles and the size of the generation domain, the concentration of solids was significantly lower compared to the real process to simplify further contact detection and analysis.

Since the force-biased algorithm is used for the initial placement, the particles in the generated scene may have slight overlaps. They are usually very small (less than 1% of the radius) and therefore have no noticeable effect on the initial particle velocity. Yet, to avoid this effect completely, the sizes of all particles were artificially increased by 5% during generation, and then returned to their original size before starting the simulation. This allowed us to obtain the initial scenes without any particle intersections. The initial velocities of the particles were set equal to the corresponding flow velocities according to their Z coordinates (see Appendix A.1.2).

In the real process, particles are agglomerated with a change in their size. Nevertheless, to reduce the computational effort, the diameters of the objects were kept constant during the simulation, so no actual particle fusion or breakage was modeled. Instead, only the contacts between particles, built due to cohesive forces, were analyzed. Therefore, the growth of granules was simulated indirectly, by introducing particles of different sizes into the simulation, which could collide, forming particles of other transitional diameters. By introducing particles of multiple sizes, it was possible to simulate a quasi-continuous growth of granules. In overall, the particles of 19 fixed sizes between 0.08 μm and 1.8 μm were modeled. Aggregates consisting of several particles make it difficult to collect statistics, so only binary ones were considered. Therefore, only a limited time interval could be meaningfully simulated before the particles form larger agglomerates of three or more objects. It was allowed only about 5% of objects to have non-binary contacts, otherwise, the statistics were considered unreliable. Thus, the total simulation time for each case was limited to 0.011 s. Given this restriction, each simulation was repeated three times, which was a compromise between simulation time and the amount of collision statistics collected.

The maximum allowed simulation time step was limited by the applied diffusion model [41] and was equal to

$$\Delta t_{sim,crit,diff} = \frac{2\rho_{sol}r_{part,min}^2}{9\eta_{max}} = 3.26 \times 10^{-10} \text{ s}, \quad (1)$$

where ρ_{sol} is the density of particles, $r_{part,min}$ is the minimum radius of particles on the scene, and η_{max} is the maximum fluid viscosity over all investigated case studies.

On the other hand, the critical simulation step for DEM is usually calculated in terms of the Rayleigh step Δt_R [43], which depends on the particle size and the mechanical properties of the material, in particular, Young's modulus and Poisson ratio. Usually, 10–20% of Δt_R is used as the simulation time step. With realistic values of mechanical properties of the modeled material, this evaluates to a critical step

$$\Delta t_{sim,crit,R} < 1 \times 10^{-11} \text{ s}, \quad (2)$$

which is quite small, causing long simulation times. Therefore, in order to speed up the computations, Young's modulus E of the particles was reduced to fit 20% of the critical time step for the diffusion model and back-calculated as:

$$E = \left(0.2 \frac{\pi r_{part,min} \sqrt{2\rho_{sol}(1+\nu)}}{\Delta t_{sim,crit,diff}(0.1631\nu + 0.8766)} \right)^2, \quad (3)$$

where ν is the Poisson ratio of particles. This made it possible to use a time step that, on the one hand, satisfies the limitations of the diffusion model, and, on the other hand, provides an acceptable duration of each simulation.

According to all these considerations, the following material and simulation parameters (Table 2) have been applied for all DEM runs.

Table 2. Parameters used in DEM simulations.

Parameter		Value	Units
Density	ρ_{sol}	2200	kg m^{-3}
Young's modulus	E	39.7	MPa
Poisson ratio	ν	0.3	-
Restitution coefficient	e_{rest}	0.05	-
Sliding friction	μ_{sl}	0.05	-
Radius	r_{part}	0.08...1.8	μm
Particles number		50,000	-
PBC size		43.211	μm
Simulation time step	Δt_{sim}	2×10^{-10}	s
End simulation time	t_{end}	0.011	s

All DEM simulations were performed in the open-source framework MUSEN [44], applying GPU-accelerated computations. The general view of the DEM scene at the end of the simulation with the particle velocity distribution is given in Figure 3. The total CPU time spent to calculate all 3×1200 simulations was about 670 days.

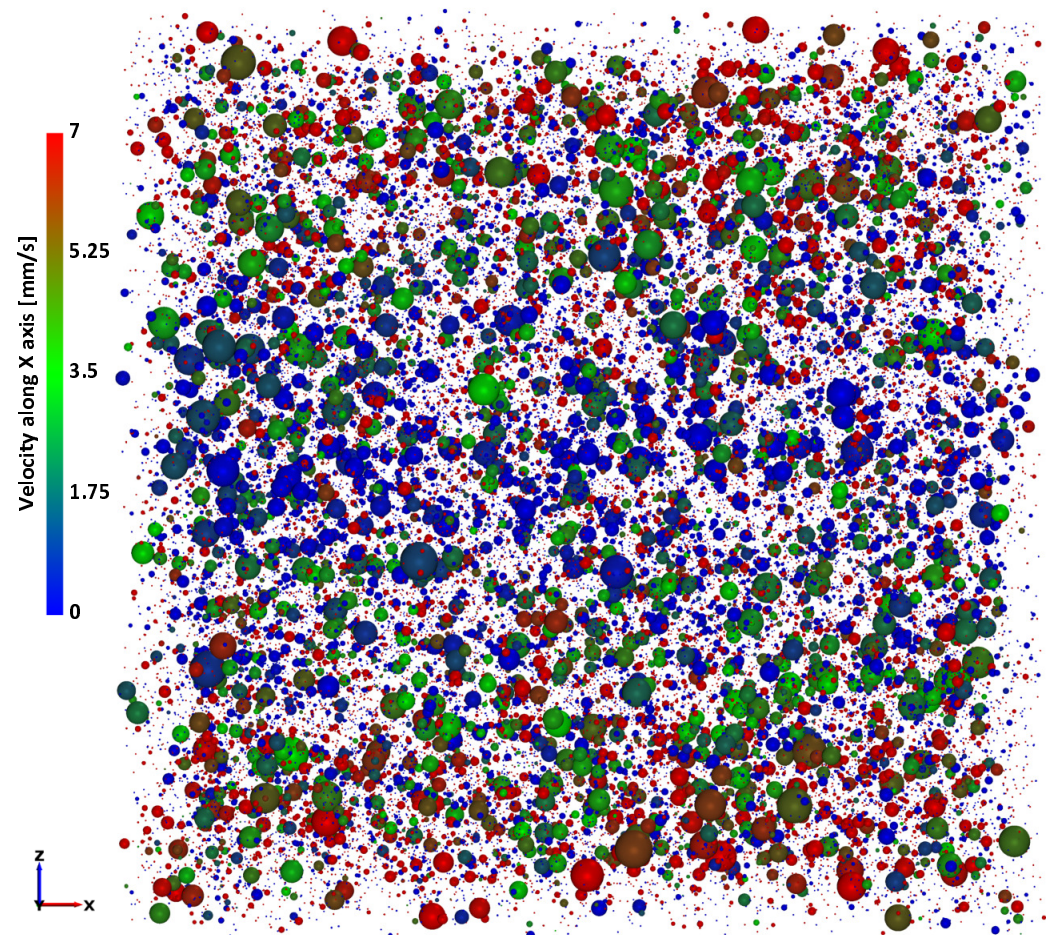


Figure 3. General view of one of the simulated DEM scenes at time 0.011 s. The color of the particles corresponds to their speed along the X axis, caused by both shear and Brownian motion.

2.1.3. Data-Driven Model

Cohesive contacts between particles can continuously appear and disappear during the simulation. In order to select only those events that led to actual agglomeration, 3 time

points were analyzed for each case: 0 s, 0.01 s and 0.011 s, and the final contacts sets C were calculated as

$$\{C\} = (\{C(0.01)\} - \{C(0)\}) \cap \{C(0.011)\}. \quad (4)$$

At first, all contacts that have arisen during the analyzed time interval of 0.01 s were determined, and then those that were not long-term ones and disappeared at the end time point 0.011 s were removed from the set.

To compensate for the effect of reduced density and different numbers of particles of each size, the number of contacts were further scaled by the number of particles as

$$C_{norm,ij} = \frac{C_{ij}}{N_i N_j}, \quad (5)$$

where C_{ij} is the number of contacts between particles of size i and j , N_i and N_j are the total number of those particles, respectively. In addition, due to the limited amount of data, they had to be further filtered to smooth out individual outliers.

The overall agglomeration behavior β_{Su} was estimated as a composition of Brownian β_{Br} and Shear β_{Sh} agglomeration kernels:

$$\beta_{Su} = \beta_0(k_{Br} \cdot \beta_{Br} + k_{Sh} \cdot \beta_{Sh}), \quad (6)$$

$$\beta_{Br} = \beta_{0,Br} \left(v^{\frac{1}{3}} + u^{\frac{1}{3}} \right) \left(v^{-\frac{1}{3}} + u^{-\frac{1}{3}} \right), \quad (7)$$

$$\beta_{Sh} = \beta_{0,Sh} \left(v^{\frac{1}{3}} + u^{\frac{1}{3}} \right)^3, \quad (8)$$

where u and v are particle volumes, and β_0 , $\beta_{0,Br}$, and $\beta_{0,Sh}$ are size-independent agglomeration rate constants. The values of kernel coefficients k_{Br} and k_{Sh} were estimated from the extracted collisions statistics using GlobalSearch optimization algorithm with `fmincon` solver from MATLAB. Thus, each sample of parameters in the range from Table 1 was assigned two coefficients: k_{Br} and k_{Sh} .

These values were used to train an artificial neural network model applying TensorFlow library [45] used via Keras python interface [46]. For each kernel coefficient, a separate multilayer perceptron with four inputs, one output, and several hidden dense layers has been created. To train the network, the Adam optimization algorithm [47] with the mean squared error as the loss function was used. To design and set up the parameters of the model in an optimal way, KerasTuner hyperparameter optimization framework has been utilized with the validation loss as the objective function. It was allowed to change the following values: number of hidden layers (1 to 6), number of neurons (8 to 64), and activation functions (relu, sigmoid, softmax, tanh) for each layer, and the learning rate of Adam's algorithm. The final obtained configurations were as shown in Table 3. For both models, a learning rate of 0.01 was selected.

Table 3. Configurations of the obtained ANN models.

Layer	Brownian		Shear	
	Neurons	Activation Function	Neurons	Activation Function
1	20	softmax	12	sigmoid
2	20	softmax	12	sigmoid
3	60	relu		
4	52	tanh		
5	12	tanh		

For the obtained ANN configurations, additional studies were carried out to determine the optimal number of training epochs, also using KerasTuner. They showed that the best number for Brownian and shear neural networks is 235 and 193, correspondingly. These settings were used to train the final models.

Before training the models, 10 outliers with a z-score greater than 2.7 were removed from the entire set of input data. For subsequent testing of the obtained models, 100 samples were excluded from the remaining ones, making up the test set. Additionally, to avoid overfitting, the cross-validation principle was used by splitting the available data set into validation and training subsets in proportion of 3:7. Thus, considering all of the above, the sizes of the sets were as follows:

- Training set: 763 samples;
- Validation set: 327 samples;
- Testing set: 100 samples.

The final trained models were exported as a C++ module using the keras2cpp library [48] for further integration within the flowsheet simulation framework Dyssol.

2.1.4. Macroscale Model

The obtained ANN were used as surrogate models, allowing easily linking process parameters and the agglomeration kernel. On their base, a macroscale population balance model was designed and implemented in the flowsheet simulator Dyssol as a batch unit.

The reaction model of the zeolite synthesis describes the transformation of initial reagents $M1$, $M2$, and $M3$ into unit cells UC . The resulting unit cells precipitate in the form of X-ray amorphous particles, which in turn transform into crystalline particles. Thereafter, the crystalline particles are agglomerated until the final particle size is reached. Additionally, organic templates Te are usually used [10] to control the formation of the porous structure of the final product by providing a surface, where the nucleation process can start. In general, the reactions taking place in the apparatus can be described by the following simplified scheme:



where v_i is the stoichiometric coefficient of the corresponding reactant i .

The time-dependent change in concentration of all materials is described as:

$$\frac{dc_{M1}}{dt} = -v_{M1}r_1, \quad (11)$$

$$\frac{dc_{M2}}{dt} = v_{M1}r_1 - v_{M2}r_2, \quad (12)$$

$$\frac{dc_{M3}}{dt} = -v_{M3}r_2, \quad (13)$$

$$\frac{dc_{UC}}{dt} = r_2 - \frac{\dot{n}_{Am}}{V_{tot}N_{UC}}, \quad (14)$$

$$\frac{dc_{Te}}{dt} = -v_{Te}r_2, \quad (15)$$

where V_{tot} is the total volume of the solution, \dot{n}_{Am} is the number of formed X-ray amorphous particles per unit time, and N_{UC} is the number of UC moles per zeolite particle.

The kinetics of the first reaction (Equation (9)) is calculated according to the Arrhenius equation, which leads to the following expression for the reaction rate:

$$r_1 = k_1 \exp\left(\frac{-E_A}{RT}\right) c_{M1}^{n_{M1}}. \quad (16)$$

Here, E_A denotes the reaction activation energy, R is the universal gas constant, T is the temperature, k_1 is the dissolution constant for reaction 1, c_{M1} is the molar concentration of $M1$, and n_{M1} is the fitting parameter. Experimental data on the compounds concentration were used to estimate the required kinetic parameters.

Based on the experimentally obtained concentrations, the rate of the second reaction (Equation (10))—the formation of unit cells—was estimated as

$$r_2 = k_2 c_{M2}^{n_{M2}} c_{M3}^{n_{M3}} c_{Te}^{n_{Te}}. \quad (17)$$

Here, the values n_i are fitting parameters, and k_2 is the pre-exponential factor of the second reaction.

The population balance of crystalline and X-ray amorphous particles describes the change in their numbers N as:

$$\frac{dN_{Am}}{dt} = \dot{n}_{Am} - \dot{n}_{Cr}, \quad (18)$$

$$\frac{dN_{Cr}}{dt} = \dot{n}_{Cr}. \quad (19)$$

The kinetics of the formation of X-ray amorphous particles and their transformation into crystalline particles are modelled using a self-accelerating kinetic approach, as shown in the equations:

$$\dot{n}_{Am} = (k_{Am,1} + k_{Am,2} N_{Am}^{n_{Am,1}}) c_{UC}^{n_{UC}}, \quad (20)$$

$$\dot{n}_{Cr} = (k_{Cr,1} + k_{Cr,2} N_{Cr}^{n_{Cr}}) N_{Am}^{n_{Am,2}}, \quad (21)$$

where k_i and n_i are fitting coefficients.

To parametrize the concentration and number balances, experiments and resolved CFD simulations were used. Here, a laboratory-scale reactor with about 1.5 million cells, and a production-scale reactor with approximately 10 million cells were simulated in ANSYS Fluent. A polyhedral mesh with boundary layers and with mesh refinement at the locations with high shear rates was applied for both geometries. The calculations for the laboratory scale were laminar, transient, and used sliding mesh for the stirrer zone. For the production scale, calculations were performed stationary with the k-omega turbulence model and frame motion. For transient calculations, to ensure that the initial values do not influence the outcome, at least 10 revolutions of the stirrer were always simulated before the results were evaluated for one revolution.

In order to initiate the particle growth, all newly emerging crystalline particles (Equation (21)) were assigned the size D_{new} , defined as a model parameter. The particle growth due to agglomeration is given by Equation (22), where $\beta_{Su}(u, v)$ is the agglomeration kernel, calculated with the previously described surrogate model, and β_0 is the agglomeration rate constant. Fixed pivot technique [49] was used to numerically solve Equation (22).

$$\frac{\partial n(v, t)}{\partial t} = \beta_0 \beta_0(u, v) \left(\frac{1}{2} \int_0^v \beta_{Su}(u, v-u) n(u, t) n(v-u, t) du - \int_0^\infty \beta_{Su}(u, v) n(u, t) du \right). \quad (22)$$

It was found that the resulting model overpredicts the final particle sizes since it lacks an agglomeration stopping criterion. Further investigations are needed to establish the physics of this process. To overcome this shortcoming in the current implementation, the PBM model was extended with a size-dependent agglomeration rate coefficient $\beta_0(u, v)$:

$$\beta_0(u, v) = \begin{cases} 1 & , (u+v) < k_{uv1}, \\ \frac{k_{uv1} - (u+v)}{k_{uv1} - k_{uv2}} & , k_{uv1} \leq (u+v) \leq k_{uv2}, \\ 0 & , (u+v) > k_{uv2}, \end{cases} \quad (23)$$

with fitting parameters k_{uv1} and k_{uv2} .

2.2. Decanter Centrifuge

After synthesis, the generated particulate matter is enriched by a solid–liquid separation step to achieve a sufficiently high solids content for the subsequent step of spray drying. In this case study, a continuously operating decanter centrifuge separates the synthesized solid material from the liquid phase. The physical principle of separation for this type of centrifuge lies in the existing density difference between the particulate solid and the continuous liquid phase. The main parts of a decanter centrifuge are a cylindrical-conical bowl, a screw conveyor, a feed pipe, an overflow weir, and a drive system (Figure 4).

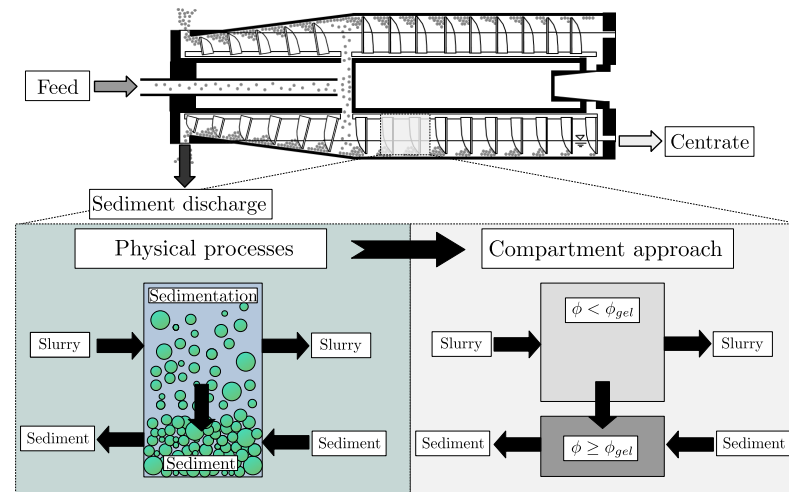


Figure 4. **Top:** Schematic representation of a counter-current decanter centrifuge considering a cylindrical-conical bowl, a screw conveyor system and a feed pipe. **Bottom:** Separation related properties and interconnection of slurry and sediment for a single compartment. ϕ is the volume fraction of the solid phase and ϕ_{gel} is the gel point.

A pump conveys the slurry via the feed pipe into the machine. The decanter centrifuge works on the counter-current principle. This means that the slurry flows in the direction of the overflow weir and the conveyor system transports the formed sediment in the opposite direction. Due to the rotating bowl, the centrifugal force acts on the suspension and a pre-acceleration occurs at the transition between the cylindrical and conical parts of the decanter centrifuge. The centrifugal force acts on the slurry and forms the rotating liquid pond with the height of approximately the overflow weir. Solid particles have a higher density than the liquid and settle towards the inner wall of the bowl, forming a liquid-saturated sediment. Once the sediment is sufficiently compacted, the screw conveyor, which rotates with a small speed difference relative to the cylindrical-conical bowl, transports the material towards the conical part. Here, the sediment is ejected from the machine.

2.2.1. Model Structure

The dynamic model of the decanter centrifuge takes into account the sedimentation behavior, the sediment build-up of liquid-saturated bulk material with compressible behavior, and the sediment transport. The interconnection of individual ideally mixed compartments, as summarized in Figure 5, forms the structure of the dynamic model.

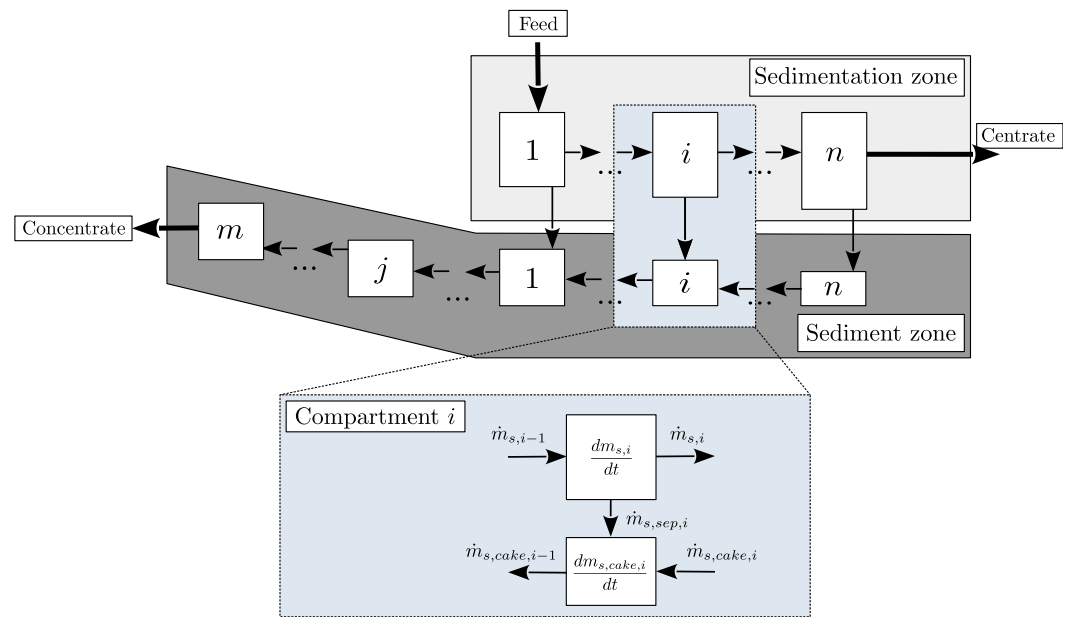


Figure 5. Schematic representation of the structure of the multi-compartment model of a counter-current decanter centrifuge.

The dynamic model divides the compartments into the sedimentation zone and the sediment zone. While the sedimentation zone represents the free flow of slurry in the machine, the sediment zone models the sediment build-up and transport. According to Menesklou et al. [50], compartment interconnection of the sedimentation and the sediment zones allows us to predict process dynamics and the change in particle size distribution and solids content along the unrolled screw channel. Since this is a macroscopic modeling for use in the flowsheet simulation, assumptions and simplifications of the real process are necessary. A detailed discussion about the assumptions made can be found in Gleiss et al. [33].

2.2.2. Model Equations

Sedimentation Zone

The stationary component balance for the relevant particle size considers the change of particle size distribution in each compartment i :

$$\dot{m}_{s,i-1}q_{3,i-1}(x) = \dot{m}_{s,i}q_{3,i}(x) + \dot{m}_{s,sep,i}q_{3,sep,i}(x). \quad (24)$$

Here, $q_{3,i}$ and $q_{3,sep,i}$ are mass-related density distribution of particle size in the material flowing out of the compartment i to the next sedimentation compartment and to the sediment compartment, respectively; $\dot{m}_{s,i-1}q_{3,i-1}(x)$ and $\dot{m}_{s,i}q_{3,i}(x)$ are the amount of particles of size x flowing into and out of the compartment i ; and $\dot{m}_{s,sep,i}q_{3,sep,i}(x)$ is the amount of particles of size x separated by centrifugal force. The change in total solids mass for each compartment is calculated as follows:

$$\frac{dm_{s,i}}{dt} = \dot{m}_{s,i-1} - \dot{m}_{s,i} - \dot{m}_{s,sep,i}. \quad (25)$$

The accumulation term of the solids mass $\frac{dm_{s,i}}{dt}$ depends on the incoming solids mass flow $\dot{m}_{s,i-1}$, the outgoing solids mass flow $\dot{m}_{s,i}$ and the deposited solids mass flow $\dot{m}_{s,sep,i}$.

In order to solve the component balance of the solids phase, it is assumed that it is back-mixed in each compartment and the amount of separated solids can be described as a time-dependent separation efficiency,

$$E_i(t) = \frac{\dot{m}_{s,sep,i}}{\dot{m}_{s,i-1}}. \quad (26)$$

The separation efficiency depends on the ratio of separated to incoming solid particles. Additionally, the integration of the feed density distribution and grade efficiency T along the integration borders x_{min} and x_{max} allows us to calculate the separation efficiency in a compartment:

$$E_i(t) = \int_{x_{min}}^{x_{max}} T_i(x, t) q_{3,i-1}(x) dx. \quad (27)$$

For direct calculation of the change in the volume fraction of solids in a compartment, the transformation of the unsteady mass balance (Equation (25)) into a volume balance is carried out considering Equations (26) and (27):

$$V_i \frac{d\phi_i}{dt} = \dot{V}_{i-1} \phi_{i-1} \left[1 - \int_{x_{min}}^{x_{max}} T_i(x, t) q_{3,i-1}(x) dx - \frac{\dot{V}_i \phi_i}{\dot{V}_{i-1} \phi_{i-1}} \right], \quad (28)$$

where ϕ is the volume fraction of the solid phase.

The grade efficiency, assuming a homogeneous distribution of particles over the entire flow cross-section, can be obtained from the geometric quantities, process settings and material properties as follows:

$$T_i(x) = \frac{R_{s,i}(t)}{R_{s,i}(t) - R_w} \left[1 - \exp \left(- \frac{\Delta\rho h_i x^2}{18\eta_l} \frac{\omega^2}{\dot{V}_{i-1}} \frac{[R_{s,i}(t) - R_w] B_k \Delta L}{1} \right) \right]. \quad (29)$$

Here, $R_{s,i}(t)$ is the radius of the sediment surface, R_w is the radius of the overflow weir, $\Delta\rho$ is the density difference between solid and liquid, h_i is the time-dependent hindered settling function, x is the particle diameter, η_l is the dynamic viscosity of pure liquid, ω is the angular velocity of the centrifuge bowl, \dot{V}_{i-1} is the volume flow of the slurry, B_k is the screw pitch and ΔL is the discretized length of the unrolled screw channel. At the beginning, $R_{s,i}$ is equal to the bowl radius R_b . The hindered settling function is defined as:

$$h_i = p_1 \left(1 - \frac{\phi_{s,i-1}}{\phi_{sed,max}} \right)^{p_2} + p_3, \quad (30)$$

where p_1 , p_2 , p_3 , and $\phi_{sed,max}$ are model parameters.

The equations of the sedimentation zone apply only to the cylindrical part of the bowl.

Sediment Zone

The sediment zone includes the formation of sediment and the transport of liquid-saturated sediment towards the solids discharge. The transition between the sedimentation zone and the sediment zone is modeled by the gel point ϕ_{gel} . Analogous to the sedimentation zone, the solids mass balance can be established for the sediment zone:

$$\frac{dm_{s,cake,i}}{dt} = \dot{m}_{s,cake,i} - \dot{m}_{s,cake,i-1} + \dot{m}_{s,sep,i}. \quad (31)$$

Here, $m_{s,cake,i}$ is the accumulated solids mass in the sediment, $m_{s,cake,i-1}$ and $m_{s,cake,i}$ are the solids mass streams of transported material. The volume flow of the transportable sediment,

$$\dot{V}_{s,cake,i} = \bar{\phi}_{cake,i} A_{cake,i} \bar{v}_{tr}, \quad (32)$$

is the product of the volume-averaged solids volume fraction $\bar{\phi}_{cake,i}$ in the sediment and the cross-sectional area $A_{cake,i}$ of the sediment, as well as the average transport velocity \bar{v}_{tr} . The

cross-sectional area $A_{cake,i}$ of the sediment in the unrolled screw channel can be calculated from the side lengths B_k and $R_b - R_{s,i}(t)$. Transforming mass conservation (Equation (31)) to a volume balance and substituting Equation (32) yields the final form of the equation to calculate the sediment transport in compartment i :

$$\frac{dm_{s,cake,i}}{dt} = E_i(t)\dot{m}_{s,i-1} + \rho_s \bar{v}_{tr} [\bar{\phi}_{cake,i} A_{cake,i} - \bar{\phi}_{cake,i-1} A_{cake,i-1}]. \quad (33)$$

The solids transport velocity depends on the the differential speed Δn between the screw and the bowl, the screw pitch angle α and the material behavior, which is described by the transport efficiency k , and is given as follows:

$$\bar{v}_{tr} = \frac{k B_k \Delta n}{\sin \alpha} \begin{pmatrix} 1 \\ \cos \delta \end{pmatrix}. \quad (34)$$

The efficiency of the sediment transport is a crucial parameter, which depends on the material behavior as well as on the geometry of the screw and the process conditions. In the conical part, the cone angle leads to a decrease in the transport velocity, which is why Equation (34) for the conical part must take into account the intersection angle δ .

Additional geometric consideration are given in Appendix A.2. In addition to the equations presented, models and material functions (e.g., settling behavior, sediment compression, shear compaction, transport efficiency) are required to calculate particle settling and sediment formation process and the volume of each compartment in the sedimentation zone. At this point, for a detailed description of the equation system for the dynamic model of the presented decanter centrifuge, the readers are referred to the already-published work [32–34,50].

2.3. Spray Dryer

A multi-compartment approach is used to model the co-current spray drying process by discretization along the dryer's vertical axis, according to the work of Buchholz et al. [35]. The model structure is schematically shown in Figure 6. In each dryer compartment, the suspension droplets before and after solidification are treated as a granular phase which is described by a two-dimensional population balance approach according to the particle size and water mass fraction. The model considers the heat and mass transfer between the gas and the particles, as well as the heat loss over the dryer wall. In each compartment, the respective phases are treated as ideally mixed. Due to negligible transient behavior, the system is modeled as quasi-stationary. The respective balance and constitutive equations are summarized in [35].

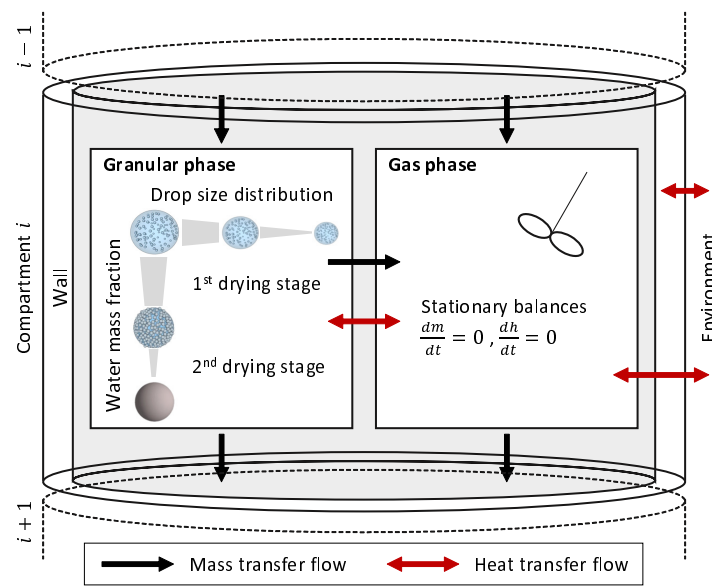


Figure 6. Model structure of a co-current spray drying process with compartmentalization along the vertical axis. In each compartment, the mass and heat transfer between the gas, granular, and wall phases are considered. A two-dimensional population balance approach allows for the consideration of the different drying kinetics before and after solidification.

2.4. Rotary Kiln

The structure of the rotary kiln model is based on the works of Martins et al. [51], Küssel [36], and Ginsberg et al. [52]. As shown in Figure 7, the kiln is divided along its horizontal axis into multiple compartments that consist of the following phases: gas (g), solid (s), and wall (w). Gas and solids move in opposite directions through the rotating kiln. The heat transfer between wall, solids, and gas phase is dominated by different heat transfer mechanisms which lead to a circumferential temperature profile in a thin layer of the inner kiln wall. Therefore, the inner part of the wall is divided into two distinct regions, i.e., a solid-wall (ws) and a gas-wall (wg) interface region. The kiln is externally heated on the outside of the wall to provide the energy needed to dry out the remaining water in the solid phase and to heat the substance to the temperature needed to start the exothermic combustion reaction.

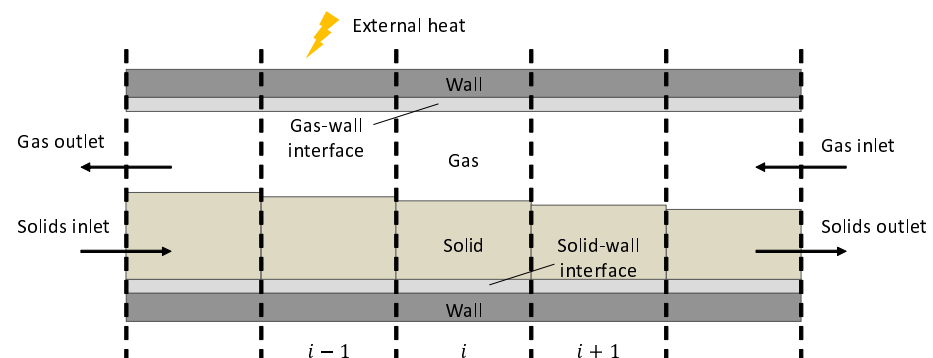


Figure 7. Structure of a multi-compartment rotary kiln model describing a counter-current calcination process. Three different phases are considered: gas, solid and wall. The system is externally heated via the kiln wall.

In Figure 8, the mass and heat flows between the different phases and regions are shown. The exchange mass flows between the solid and the gas phase in each compartment occur due to the evaporation of water and due to the combustion reaction. This leads to a mass flow of O_2 from gas to solid and a mass flow of the reaction product—in this case

CO₂—from the solid to the gas phase. While the gas flows only in one direction, there is a backward-directed solids flow that accounts for possible back-mixing effects inside the particle bed. The amount of back-mixing and the overall particle velocity in the axial direction depend on the filling, the rotational speed, and possible internal structures inside the kiln. As the model does not describe this particle motion in detail, the information on the particle movement is taken from high-resolution CFD-DEM simulations of the whole kiln.

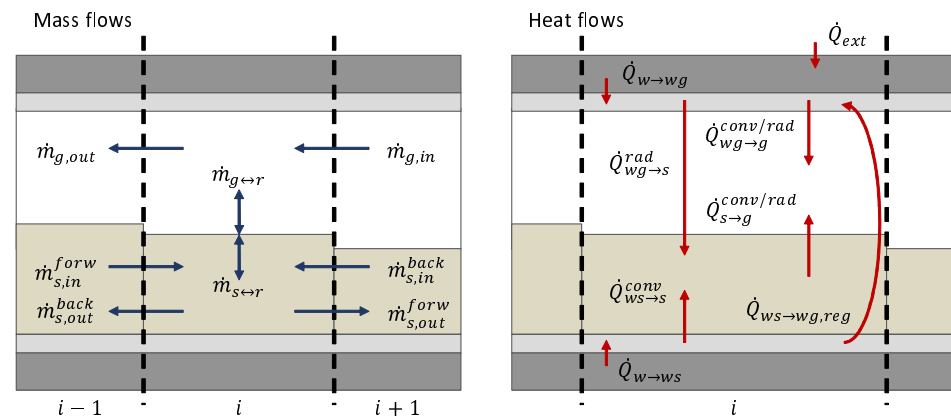


Figure 8. Modelled mass flows between the phases and the compartments (left) and heat flows due to different transfer mechanisms between the phases (right).

The heat transfer between the walls and solids is dominated by convection on the solid–wall interface due to the rotation. Additionally, the convective heat transfer between gas and solid and between gas and wall is described. The heat transfer via radiation is modeled between the gas–wall interface and the gas and the solid surfaces. Due to the rotation of the wall and the different temperatures of the respective wall interfaces, there is an enthalpy flow, also called regenerative heat transfer, between both wall regions. The external heat is conducted via the wall region towards the wall interface regions. Axial heat transfer is neglected.

In the following section, the mass and enthalpy balances that describe the phases of a single compartment are presented. The constitutive equations for the calculation of the heat and mass transfer are given in Appendix A.3.

2.4.1. Solid Phase

In the solid phase, three compounds are present: an inert zeolite compound, an organic compound that is represented by pure carbon, and the remaining water after the drying process. The overall mass balance for the solid phase, which takes into account the forward and backward movement of the solid material as well as the mass exchange with the gas phase, reads as follows:

$$\frac{dm_s}{dt} = \dot{m}_{in,s}^{forw} + \dot{m}_{in,s}^{back} - \dot{m}_{out,s}^{forw} - \dot{m}_{out,s}^{back} + \sum_k^{N_k} \dot{m}_{s \leftrightarrow r,k} \quad (35)$$

with subscript r standing for reaction zone, and N_k denoting the number of reactions. The reaction terms of the solid phase $\dot{m}_{s \leftrightarrow r,k}$ depend in this case on the reaction rate of the calcination reaction and the evaporation rate.

The general compound mass balance for compound j is set up similarly to the overall mass balance:

$$\frac{dm_{j,s}}{dt} = \dot{m}_{in,j,s}^{forw} + \dot{m}_{in,j,s}^{back} - \dot{m}_{out,j,s}^{forw} - \dot{m}_{out,j,s}^{back} + \sum_k^{N_k} \dot{m}_{s \leftrightarrow r,k,j} \quad (36)$$

The calcination reaction is described by a simplified approach to the combustion reaction of an organic material, which is represented by carbon, i.e., $C^{(s)} + O_2^{(g)} \rightarrow CO_2^{(g)}$. The reaction is assumed to take place at the solid bed surface, such that the reaction rate depends mainly on the concentration of the reactants and the surface area.

The enthalpy balance takes into account the enthalpy transfer due to mass flows between compartments $\dot{m}_s h_s$, the reaction enthalpy \dot{H}_r , as well as the heat transfer with the other phases \dot{Q} as follows:

$$\begin{aligned} \frac{d(m_s h_s)_s}{dt} = & \dot{m}_{in,s}^{forw} h_{in,s}^{forw} + \dot{m}_{in,s}^{back} h_{in,s}^{back} - (\dot{m}_{out,s}^{forw} + \dot{m}_{out,s}^{back}) h_s \\ & + \sum_k^{N_k} \dot{m}_{s \leftrightarrow r,k} h_{s \leftrightarrow r,k} + K_H \sum_k^{N_k} \dot{H}_{r,k} + \dot{Q}_{g \rightarrow s} + \dot{Q}_{ws \rightarrow s} + \dot{Q}_{wg \rightarrow s}. \end{aligned} \quad (37)$$

The specific enthalpy of the reaction products $h_{s \leftrightarrow r}$ is evaluated at the mean temperature of the gas and the solid phase,

$$T_r = T_g K_T + T_s (1 - K_T). \quad (38)$$

K_T is a model parameter needed to calibrate the reaction rates according to measurements. Additionally, the reaction enthalpy \dot{H}_r is divided between both the solid and the gas phases using the constant K_H , which defines the corresponding heat shares.

2.4.2. Gas Phase

The overall mass balance and the compound mass balance for an exemplary compound j of the gas phase are given below:

$$\frac{dm_g}{dt} = \dot{m}_{in,g} - \dot{m}_{out,g} + \sum_k^{N_k} \dot{m}_{g \leftrightarrow r,k} \quad (39)$$

$$\frac{dm_{j,g}}{dt} = \dot{m}_{in,j,g} - \dot{m}_{out,j,g} + \sum_k^{N_k} \dot{m}_{g \leftrightarrow r,k,j}. \quad (40)$$

Heat exchange between gas and wall as well as between gas and solids is modeled as a combination of radiative and convective heat. The corresponding enthalpy balance of the gas phase reads as

$$\begin{aligned} \frac{d(m_g h_g)}{dt} = & \dot{m}_{in,g} h_{in,g} - \dot{m}_{out,g} h_{out,g} + \sum_k^{N_k} \dot{m}_{g \leftrightarrow r,k} h_{g \leftrightarrow r,k} \\ & + (1 - K_H) \sum_k^{N_k} \dot{H}_{r,k} - \dot{Q}_{g \rightarrow s} + \dot{Q}_{wg \rightarrow g}. \end{aligned} \quad (41)$$

2.4.3. Wall

The enthalpy balances of the wall–solid and the wall–gas interfaces are listed below:

$$m_{ws} c_{p,w} \frac{T_{ws}}{dt} = \dot{Q}_{w \rightarrow ws} - \dot{Q}_{ws \rightarrow s} - \dot{Q}_{ws \rightarrow wg,reg} \quad (42)$$

$$m_{wg} c_{p,w} \frac{T_{wg}}{dt} = \dot{Q}_{w \rightarrow wg} - \dot{Q}_{wg \rightarrow g} - \dot{Q}_{wg \rightarrow s} + \dot{Q}_{ws \rightarrow wg,reg}. \quad (43)$$

Here, T is the temperature of the corresponding wall interfaces and $c_{p,w}$ is the specific heat capacity of the wall.

2.5. Implementation Aspects

The process simulations were performed using the open-source flowsheet simulation framework Dyssol (v1.0.2, <https://github.com/FlowsheetSimulation/Dyssol-open> (accessed on 18 October 2022)).

The size of the granular material varies significantly over the production process. Therefore, in order to limit the number of classes for each individual subprocess, different grids of distributed parameters were applied for the respective units. For the synthesis and the centrifuges, the grid size was in the nanometer range. During the spray drying process, the small primary particles agglomerated and formed larger particles with sizes in the micrometer range. Moreover, the spray dryer model additionally required the distribution of particles by moisture content. Specific grid parameters are given in the corresponding appendices.

Another challenge is the connection of units operating in different modes. In particular, the synthesis reactor operates in a batch mode, so it was calculated in a separate flowsheet. Once it reached steady-state, the information about the final PSD was extracted and put as input to the solid–liquid separation process step, which was simulated with transient behavior. The following spray drying unit was described by a quasi-stationary model, which means that its calculations must converge at every time point. Therefore, to reduce the computational load, after the transient centrifugation process, the number of output time points was reduced to about 1 point per 10–100 s.

3. Results

This chapter evaluates the simulation results for the synthesis and rotary kiln models, as well as for the entire zeolite production process. The evaluation and validation of the decanter centrifuge and spray dryer models can be found in previous publications: [32–34,50] and [35], respectively.

3.1. Synthesis

To verify the actual dependence of the microscale system on the varied parameters, correlation coefficients between the obtained total number of particle contacts and the process and material parameters were calculated. As an example, Table 4 shows the values of Spearman's rank correlation coefficients. They show how well a monotonic function can describe the relationship between the variables. As expected, there is a negative correlation with fluid viscosity and a positive correlation with shear rate and temperature. It should be noted that the dependence on the surface energy turned out to be unexpectedly low. The reason for this could be a rather narrow range of parameter changes or high particle velocities.

Table 4. Spearman correlation coefficients between the input ANN parameters (Table 1) and the total number of detected contacts in DEM simulations, as well as the kernel coefficients estimated from the extracted collisions statistics.

Parameter	Total Number of Contacts	k_{Br}	k_{Sh}
Temperature	0.150	0.177	0.102
Viscosity	−0.671	−0.976	−0.506
Shear rate	0.62	0.041	0.757
Surface energy	0.049	0.04	0.041

The values of the correlation coefficients between the estimated kernel coefficients k_{Br} and k_{Sh} and the process parameters make it possible to confirm the correct choice of the agglomeration kernels. The influence of the Brownian kernel is largely determined by the values of fluid viscosity and temperature, while the influence of the shear kernel mostly depends on shear rate and viscosity.

Before being embedded into the macroscale model, the trained surrogate model was evaluated using a test dataset. The results of model performance evaluation (Table 5) show very good prediction capabilities of both ANNs, while the model for Brownian kernel works slightly better.

Table 5. Evaluation results of ANN models on the test dataset.

	Brownian	Shear
Loss	0.000616	0.00665
Mean absolute error	0.019128	0.06419
Mean squared error	0.000616	0.00665
Root mean square error	0.024836	0.08155
R^2	0.988009	0.82738

The developed synthesis model with an integrated surrogate agglomeration kernel was first evaluated for a test case with the parameters given in Appendix A.4.

Figure 9 shows the concentration changes of all solid materials inside the reactor over time. The first reaction of conversion of the compound M1 to M2 (Equation (9)) is completed after about 6.5 min leading to the decrease in the concentration of M1 and the corresponding increase in M2. After that, the second reaction (Equation (10)) starts, consuming M2, M3, and the template for obtaining unit cells as a reaction product. In the given case, the second reaction is limited by the amount of M3, therefore, when its concentration drops to zero after 4 h of the process time, this reaction also stops. After that, the amount of M3 and the template remain constant, and the concentration of unit cells starts to decrease due to precipitation, resulting in the formation of final particles.

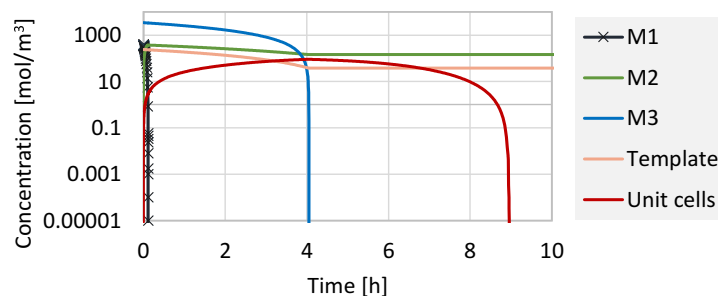


Figure 9. Change in the molar concentration of all materials during the synthesis reaction.

During the precipitation process, the X-ray amorphous particles are first formed according to Equation (18). As seen from the left side of Figure 10, the emergence of corresponding particles begins already after the appearance of the first unit cells but reaches the highest rate when the concentration of the unit cells is at a maximum. The appearing X-ray amorphous particles are consumed, forming crystalline particles (Equation (19)), which begin to grow according to the proposed agglomeration kernel (Equation (22)). The particle growth during the entire simulation time is shown in Figure 10 (right) in terms of the Sauter mean diameter. Right after all M2 is used up and the second reaction is stopped, the number of X-ray amorphous particles starts to decrease, reaching zero after about 70 h of the process time. Particle growth, in turn, stops after about 100 h, as can be seen from the progression of the Sauter diameter. At this point, a steady state is reached.

The work of the surrogate model for predicting the growth rate of agglomerates is shown by Figure 11. Here, the simulation was performed for 16 h of process time with the same simulation parameters as given in Appendix A.4 and with $\beta_0(u, v) = 1$. The parameters from Table 1 were varied independently within their ranges, substituting the corresponding values from Appendix A.4. The results obtained are in good agreement with the correlation from Table 4. Changes in surface energy and temperature have less effect

on the final agglomerate diameter compared to the influence of shear rate and viscosity. The latter, as expected, has a negative correlation with particle size, since higher viscosity values slow down particles, hindering agglomeration.

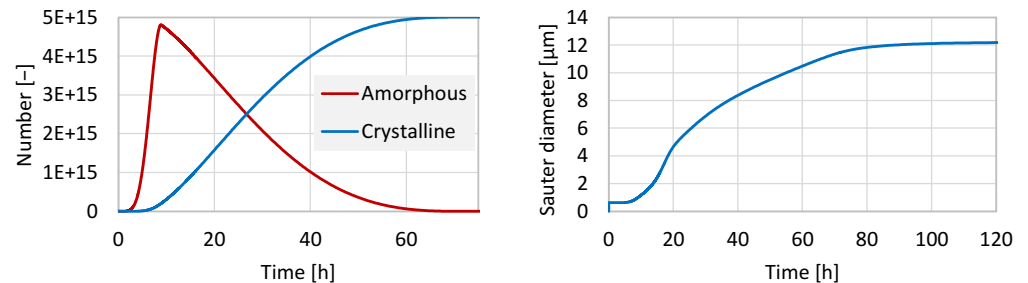


Figure 10. Change in the number of X-ray amorphous and crystalline particles (left), and in the Sauter mean diameter of agglomerating particles (left) during the synthesis.

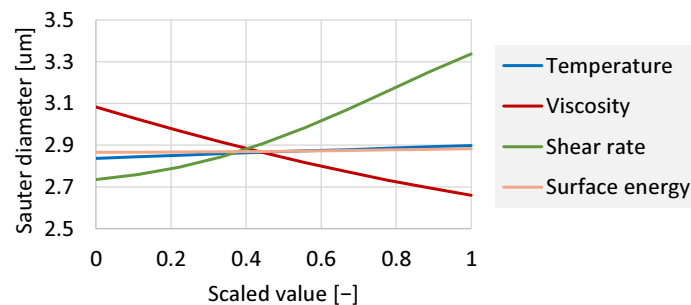


Figure 11. Influence of the ANN model input parameters on the particle growth. All parameters change in ranges as defined in Table 1 with 0 and 1 corresponding to their min and max values, respectively.

3.2. Rotary Kiln

The rotary kiln model was evaluated for four different cases, in which the heat input, expressed by the wall temperature, and the particle movement through the kiln, expressed by the Bodenstein-number, were varied as follows:

- Case A: $T_w = 850$ K, $Bo = 10^{10}$ (no back-mixing),
- Case B: $T_w = 990$ K, $Bo = 10^{10}$ (no back-mixing),
- Case C: $T_w = 850$ K, $Bo = 5$,
- Case D: $T_w = 850$ K, $Bo = 0.5$.

The remaining model parameters are given in Appendix A.5.

At first, the dynamic behavior of the granular and the gas phases was investigated for Case A. On the left-hand side in Figure 12, the change in the overall solid mass, the temperature, and the organic mass fraction of the particles along the kiln axis are shown. Evaluating the time axis of the different plots, it can be concluded that a stationary state of the process is reached after about 1 h of operation. Due to the particle acceleration and the combustion of the organic residues, the particle mass decreases along the kiln axis. A peak temperature of the particles is reached in approximately 4 m distance of the solids inlet. Thus, it can be argued that the most intense combustion reaction occurs in this place. This is confirmed by a sharp drop in the organic mass fraction.

On the right-hand side of Figure 12, the respective properties of the gas phase are shown. The gas mass in the compartments depends mainly on the density and therefore on the temperature, showing an inverted profile of the gas temperature. The drop in oxygen is located at the same distance from the solid inlet as the respective peak of the solids phase, whereas the temperature peak is slightly shifted towards the solid inlet.

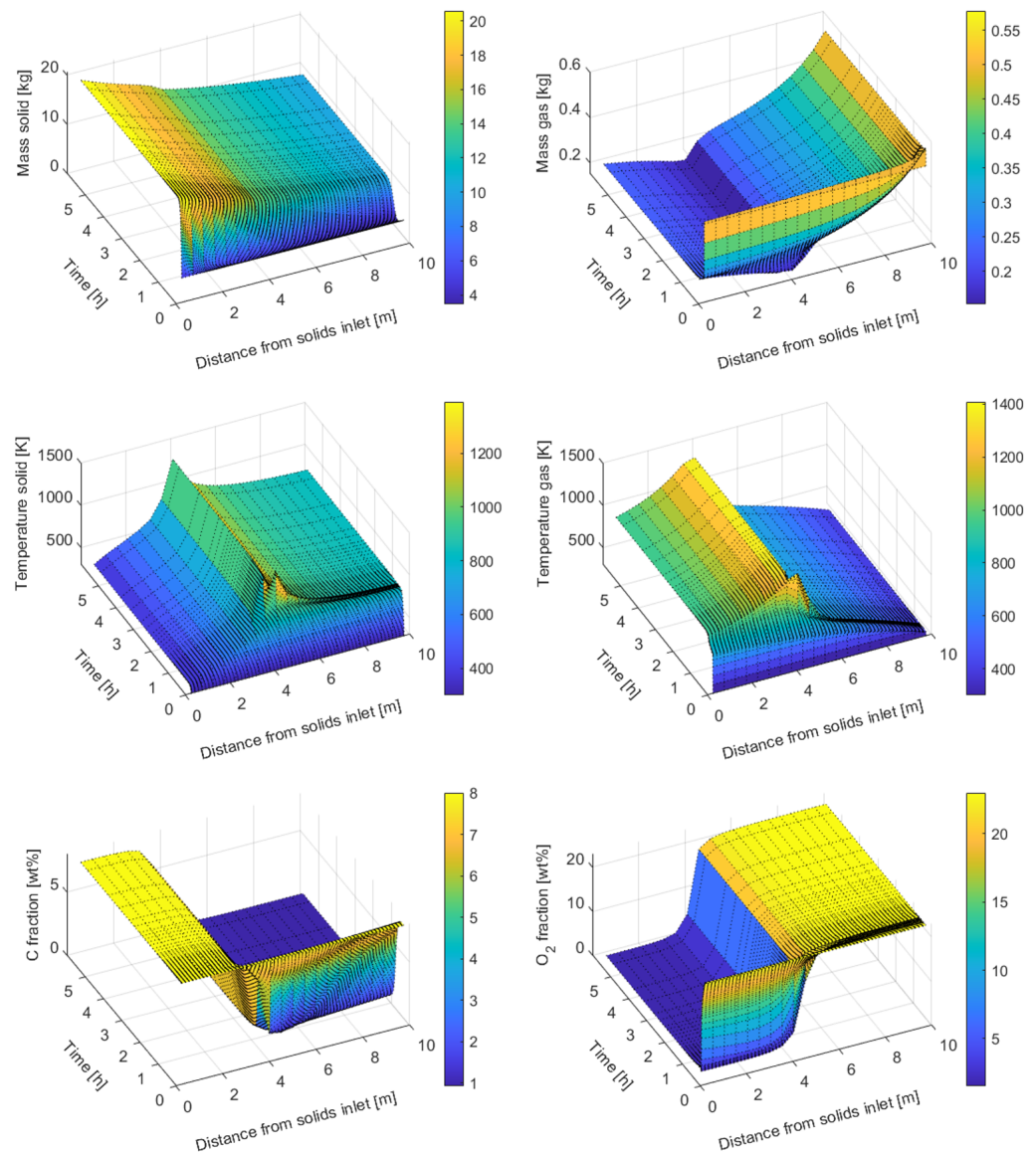


Figure 12. Time progression of solid and gas mass (**top**), solid and gas temperature (**middle**), organic residue concentration (**bottom left**), and oxygen concentration (**bottom right**) along the kiln for Case A.

The effect of changing the wall temperature and the particle back-mixing is shown in Figure 13. The increased wall temperature (Case B) has a strong impact on the reaction kinetics, allowing for a nearly complete removal of the oxygen in the gas phase and a lowered final organic mass fraction of the solids. This leads to a higher temperature peak on the one hand and to a shift of the temperature peak towards the solids outlet on the other hand, due to the counter-current flow of the gas. An increase of the back-mixing of the solids in Cases C and D leads to a shift in the solids mass distribution along the kiln towards the inlet of solid particles. On the other hand, a smoothening of the temperature peaks is observed. Additionally, an increase in the back-mixing negatively affects the combustion rate and therefore increases the residual organic mass fraction in the final product.

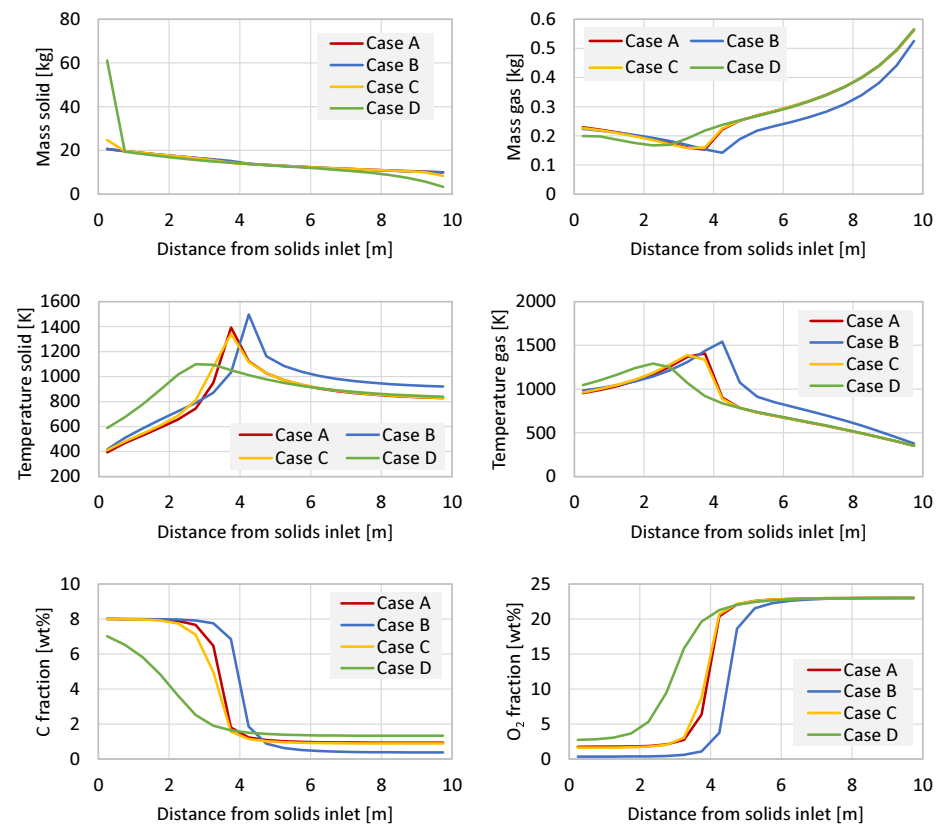


Figure 13. Influence of wall temperature and back-mixing on the simulation results. Solid and gas mass (**top**), solid and gas temperature (**middle**), organic residue concentration (**bottom left**), and oxygen concentration (**bottom right**) along the kiln after reaching steady-state.

3.3. Zeolite Production

Two different cases of the zeolite catalyst production process (Figure 1) are presented to evaluate the impact of changed operating conditions at the synthesis stage on the following process chain. The parameters of all models used in process modeling are given in Appendix A.6. As demonstrated in Figure 14, the first case shows a narrow PSD with a Sauter mean diameter of $7.1 \mu\text{m}$. For the second case, the PSD at the outlet of the synthesis stage has a Sauter mean diameter of $12.8 \mu\text{m}$ and an overall broader distribution. For both cases, a total suspension mass flow of 5400 kg h^{-1} with a solid mass fraction of 0.1 was used. The solid phase consisted of the produced zeolite material and organic residues with a mass ratio of 9:1. The organic residue in both cases was represented by pure carbon.

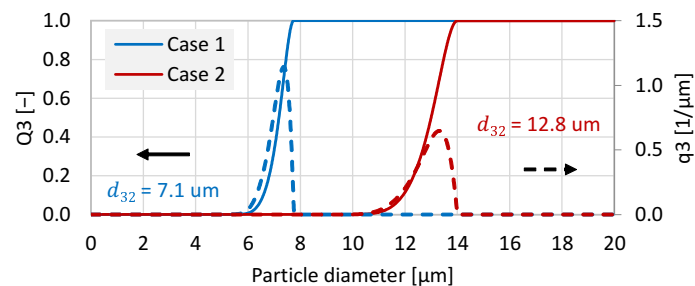


Figure 14. Cumulative and density particle size distribution and Sauter mean diameter of particles at the end of a batch process of synthesis in the reactor unit for two case studies (Suspension stream in Figure 1).

The suspension mass flow after the first centrifugation stage together with the respective solid mass fraction is shown in Figure 15. Due to the larger particles in Case 2, the centrifuge separates the particles more efficiently, leading to a higher solid mass fraction at the outlet after 1 h operation time. The suspension mass flows only show negligible deviations.

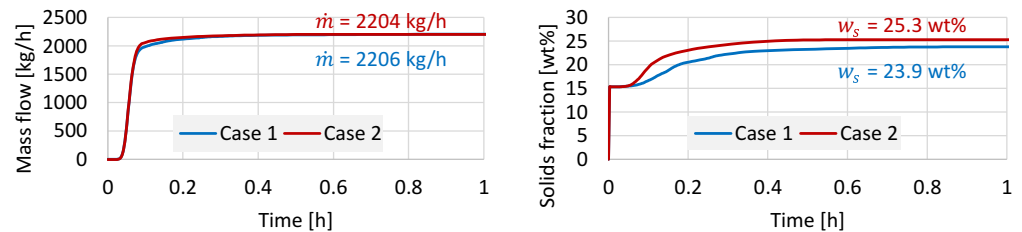


Figure 15. Time-dependent change in mass flow (**left**) and solids fraction (**right**) in the outlet stream of Centrifuge 1 (Concentrate 1 stream in Figure 1) for each case study.

After the first centrifugation stage, a washing of the suspension is performed to remove hazardous residues, such that the suspensions are diluted to 5.6 wt% and 5.93 wt% for Case 1 and Case 2, respectively. The second centrifugation step results in the mass flows and solid mass fractions shown in Figure 16. The thickened suspension, which is fed to the subsequent spray drying stage, has a water mass fraction of 17.6 wt% and 19.5 wt% for Case 1 and Case 2, respectively. As large particles experience larger centrifugal forces than smaller ones, a classification effect due to the centrifugation is expected. The resulting Sauter mean diameter of the particles after the second centrifugation stage is 7.14 μm and 12.93 μm for both cases, showing only a slight shift of the PSDs to larger particles due to separation in the centrifuge. The overall suspension mass flow is approximately 4% higher in Case 2. However, the overall solid mass flow (213.3 kg h^{-1}) there is approximately 15.2% larger than in Case 1 (185.1 kg h^{-1}), showing a significant loss of product material for Case 1 due to smaller particles.

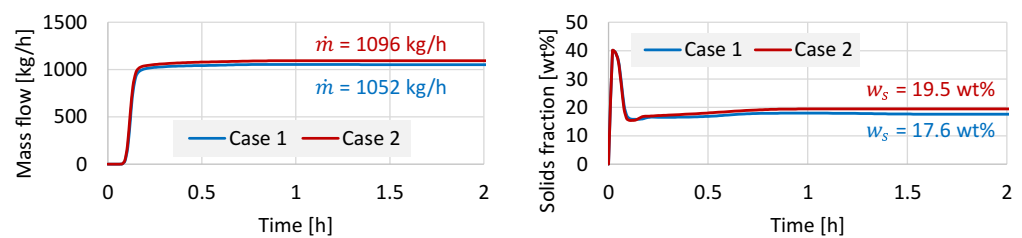


Figure 16. Time-dependent change in mass flow (**left**) and solids mass fraction (**right**) in the outlet stream of Centrifuge 2 (Concentrate 2 stream in Figure 1) for each case study.

After that, the suspension enters the drying chamber of the spray dryer through a two-fluid nozzle which creates a droplet size distribution with a Sauter mean diameter of 191 μm . In the drying chamber, the primary particles within the droplets form larger agglomerates when the droplets start to solidify. The properties of the dried particles at the spray dryer exit are shown in Figure 17. The spray dryer is affected heavily by the changes in the suspension mass flow and its composition, as the amount of water that needs to be removed from the suspension has a strong impact on the overall drying conditions. Due to the lower solid mass fraction of the suspension in Case 1, the resulting particles show a larger residue water content of 15.1 wt%. As the droplet size distribution of the atomized suspension is equal for both cases, and the moisture content for both cases falls below the critical moisture content, the particles after spray drying have the same size with a Sauter mean diameter of 0.12 mm.

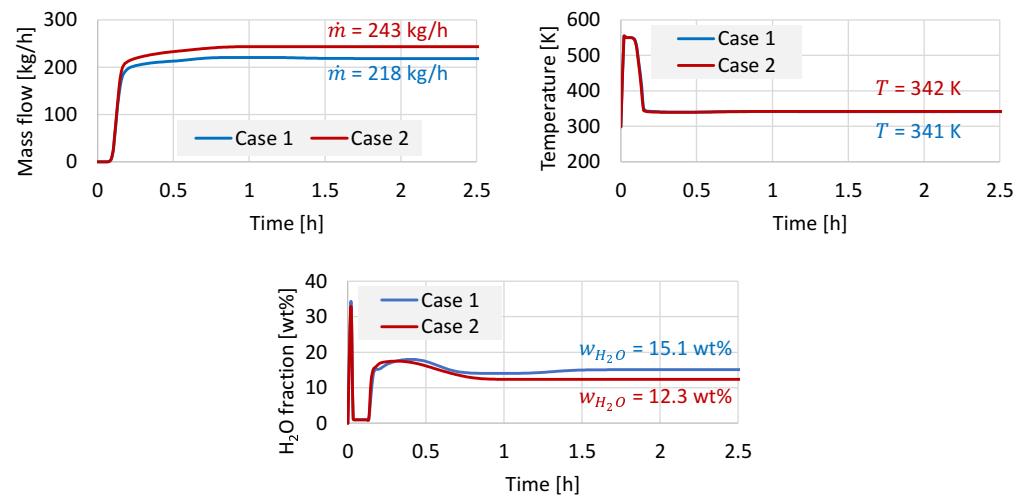


Figure 17. Time-dependent change in mass flow (top left), temperature (top right), and water content (bottom) in the outlet stream of Spray dryer (Spray particles stream in Figure 1) for each case study.

The organic residues in the solid particles are removed in two serially connected and externally heated rotary kiln stages. In the first kiln, lean air with reduced oxygen concentration is used to limit the maximum temperatures. The gas and solids properties at the respective outlets of the first kiln stage are shown in Figure 18. For both cases, the available oxygen in the lean air is nearly completely used for the combustion. As the inflow of organics, modeled as C, is too large for combustion, the solids still contain their residues. Due to a lower solids flow rate for Case 1, the available oxygen allows for a larger reduction of the organic compounds, leaving 5.7 wt% in comparison to 6.3 wt% of Case 2. However, the larger amount of water in Case 1 leads to slightly lower solids and gas temperatures at the outlet.

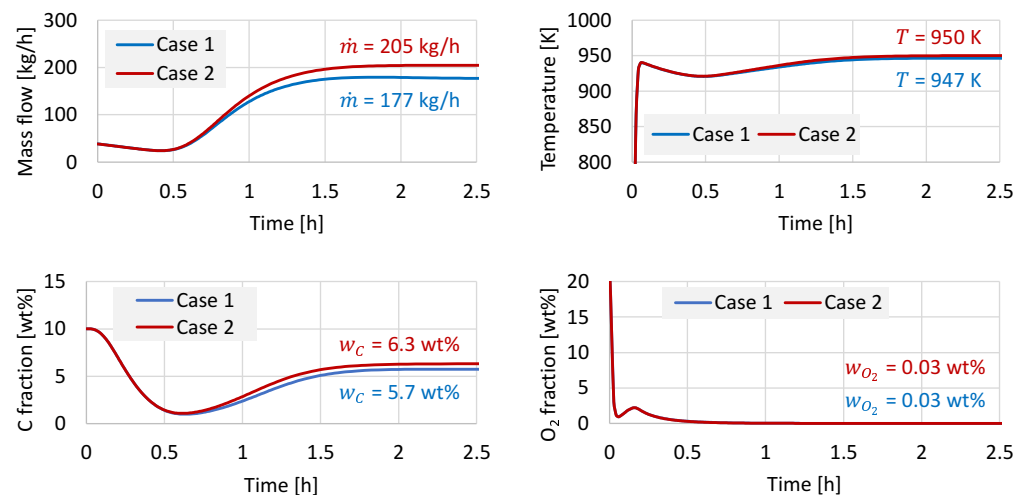


Figure 18. Time-dependent change in mass flow (top left), temperature (top right), and concentration of organic residues (bottom left) in the solids outlet stream of Calciner 1 (Particles stream in Figure 1), and change in residual oxygen concentration (bottom right) after combustion in the gas outlet stream (Out calciner gas 1 stream in Figure 1).

For the second calcination stage, ambient air with 21% oxygen is used. Gas and solids properties at the respective outlets of the second kiln stage are given in Figure 19. It is shown, that the larger amount of organic material in Case 2 leads to a lower oxygen content of the air at the outlet of the second kiln. Nonetheless, for both cases, the organic residues are completely removed from the solids after the second stage.

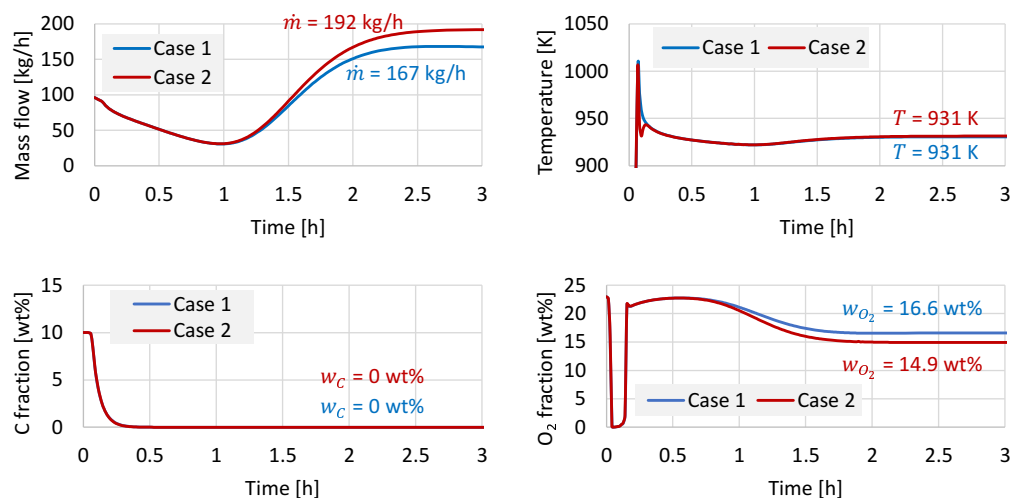


Figure 19. Time-dependent change in mass flow (**top left**), temperature (**top right**), and concentration of organic residues (**bottom left**), in the solids outlet stream of Calciner 2 (Product stream in Figure 1), and change in residual oxygen concentration (**bottom right**) after combustion in the gas outlet stream (Out calciner gas 2 stream in Figure 1).

In summary, a change of the particle size after the synthesis stage has a strong impact on the following unit operations, as it influences the efficiency of the centrifugation and therefore the following spray drying stage. In this case, two calcination stages are sufficient to remove the residual organic compounds. Additionally, they operate at similar temperatures, avoiding too large values, which may damage the product or equipment.

4. Conclusions

This work proposes a framework for modeling the industrial process of zeolite production, consisting of four stages: precipitation and agglomeration in the synthesis reactor, liquid–solid separation in a decanter centrifuge, drying in a spray dryer, and calcination in a rotary kiln.

To develop the synthesis model, a novel multiscale and multistage approach is proposed. It is based on the description of the agglomeration process using a data-driven model. Discrete element modeling is used to generate data needed to derive a reliable surrogate representation of the agglomeration kernel. Information about collisions between different particles is extracted, analyzed, and used to train the artificial neural networks. The resulting surrogate model is able to describe the growth of particles due to agglomeration, correctly taking into account the mutual influence of various process parameters such as temperature, stirring speed, liquid viscosity, and particle surface energy. Based on this, a macroscale model operating in batch mode was designed, which can be used for flowsheet simulations.

The decanter centrifuge is described with a dynamic model, which takes into account the sedimentation process and sediment accumulation, as well as compression and transport of the resulting cake in the cylindrical and conical parts of the apparatus. Here, the multi-compartment principle is applied by dividing the entire length of the centrifuge into a series of compartments, each of which describes two ideally mixed zones: sedimentation and sediment.

The co-current spray drying process is modeled using a two-dimensional population balance approach that takes into account particle size and moisture content. The obtained quasi-stationary model describes heat and mass transfer between particles, gas, and the environment.

In the calcination stage, organic substances remaining after the synthesis are removed by combustion in a rotary kiln. In the developed multi-compartment model, it is possible to take into account the backward flow of the solid phase, which describes the possible

effects of particle back-mixing. The gas moves in the direction opposite to the main flow of solids. The model is capable of describing chemical reactions at the gas–solid boundary, taking into account mass and energy balances between both phases and the kiln walls.

All obtained models were combined into a single flowsheet using the Dyssol modeling system, which allows simulation of the entire process of zeolite production. The developed framework made it possible to plausibly describe the production process, as well as to evaluate the mutual influence of various process parameters, operational conditions, and material properties on the processes occurring in each particular apparatus and, as a result, predict the properties of the final product. Moreover, the developed methods and models, as well as the entire flowsheet remain flexible, which means they can be further adjusted or fitted for use in other similar solids processes.

Author Contributions: Conceptualization: V.S., M.B., M.D., J.H., N.A., M.G., H.N., F.K.J., S.H. (Stefan Heinrich); methodology: V.S., M.B., M.D., H.K.B., M.G., G.K., D.W.; software: V.S.; validation: V.S., M.B., D.W., H.K.B., M.G., G.K.; formal analysis: V.S., M.B., M.D., H.K.B., M.G., J.H., D.W., S.H. (Simon Hammerich), G.K.; investigation: M.B., G.K., M.G., D.W., V.S., M.D.; resources: H.N., F.K.J., S.H. (Stefan Heinrich); data curation: V.S., M.B.; writing—original draft preparation: V.S., M.B.; writing—review and editing: V.S., M.B., J.H.; visualization: V.S., M.B.; supervision: H.N., F.K.J., S.H. (Stefan Heinrich); project administration: J.H., N.A., H.N., F.K.J., S.H. (Stefan Heinrich); funding acquisition: F.K.J. All authors have read and agreed to the published version of the manuscript.

Funding: Authors gratefully acknowledge the financial support of the BASF SE and the Deutsche Forschungsgemeinschaft (DFG, German Research Foundation) via project HE4526/29-1.

Acknowledgments: The authors thank Philipp Nicolas Depta for adapting and implementing the diffusion DEM model in MUSEN.

Conflicts of Interest: The authors declare no conflict of interest.

Appendix A

Appendix A.1. Synthesis

Here, the models, used for DEM simulations of the synthesis unit are described.

Appendix A.1.1. JKR Model

The contact force between each pair of particles (F_{pp}) is calculated according to the JKR model, considering both normal $F_{n,tot}$ and tangential $F_{t,tot}$ components of the force:

$$F_{pp} = F_{n,tot} + F_{t,tot}. \quad (A1)$$

The normal force is calculated as:

$$F_{n,tot} = F_{n,s} + F_{n,d}, \quad (A2)$$

$$F_{n,s} = \frac{4r_c^3 E^*}{3r^*} - \sqrt{8\pi E^* \gamma^* r_c^3}, \quad (A3)$$

$$F_{n,d} = -2\sqrt{\frac{5}{6}} \alpha v_{rel,n} \sqrt{k_n m^*}, \quad (A4)$$

where $F_{n,s}$ is the spring force and $F_{n,d}$ is the damping force, both in the normal direction.

The tangential component takes into account the sliding friction coefficient μ_{sl} and the slipping condition:

$$F_{t,s} = k_t \zeta_t, \quad (\text{A5})$$

$$F_{t,d} = -2\sqrt{\frac{5}{6}}\alpha v_{rel,t}\sqrt{k_t m^*}, \quad (\text{A6})$$

$$F_{t,tot} = \begin{cases} F_{t,s} + F_{t,d} & , |F_{t,s}| \leq \mu_{sl}|F_{n,tot}|, \\ F_{t,s}\mu_{sl}\frac{|F_{n,tot}|}{|F_{t,s}|} & , |F_{t,s}| > \mu_{sl}|F_{n,tot}|, \end{cases} \quad (\text{A7})$$

where $F_{t,s}$ is the shear component and $F_{t,d}$ is the damping component of the tangential force.

The change in the tangential overlap is calculated iteratively considering its value at the previous time point $\zeta_{t,prev}$:

$$\zeta_t = v_{rel,t}\Delta t + \kappa \frac{|\zeta_{t,prev}|}{|\kappa|}, \quad (\text{A8})$$

$$\kappa = \zeta_{t,prev} - \bar{n}(\bar{n} \cdot \zeta_{t,prev}), \quad (\text{A9})$$

where \bar{n} is the normal contact vector.

The current tangential overlap to be applied in the next iteration is calculated as

$$\zeta_{t,next} = \begin{cases} \zeta_t & , |F_{t,s}| \leq \mu_{sl}|F_{n,tot}|, \\ \frac{F_{t,tot}}{k_t} & , |F_{t,s}| > \mu_{sl}|F_{n,tot}|. \end{cases} \quad (\text{A10})$$

Used values:

$$k_n = 2E^*r_c, \quad (\text{A11})$$

$$k_t = 8G^*r_c, \quad (\text{A12})$$

$$r_c = \sqrt{\zeta_n r^*}, \quad (\text{A13})$$

$$\alpha = \frac{\log(e_{rest})}{\sqrt{\pi^2 + \log(e_{rest})^2}}. \quad (\text{A14})$$

Here, r_c is contact area radius; r^* is equivalent contact radius; E^* is equivalent Young's modulus; G^* is equivalent shear modulus; γ^* is equivalent surface energy; $v_{rel,n}$ and $v_{rel,t}$ are relative velocity of contacting particles in normal and tangential directions; m^* is equivalent mass; e_{rest} is restitution coefficient; ζ_n and ζ_t are overlaps in normal and tangential directions.

Appendix A.1.2. Diffusion Model

To simulate Brownian and shear motion, the following equations are applied for each particle:

$$F = F_{fluct} - F_{drag} + F_{lift}. \quad (\text{A15})$$

The fluctuating force F_{fluct} is defined as

$$F_{fluct} = \Omega \sqrt{m_{part}k_B T(1 - e^{-2\psi})} \frac{1}{\Delta t}, \quad (\text{A16})$$

$$\psi = 6\pi\eta \frac{r_{part}}{m_{part}} \Delta t, \quad (\text{A17})$$

where Ω is the normally distributed random number with mean 0 and standard deviation 1; m_{part} and r_{part} are particle mass and radius, respectively; k_B is the Boltzmann constant; η and T are dynamic viscosity and temperature of the liquid; Δt is the DEM integration time step.

The drag part of the force F_{drag} is calculated by

$$F_{drag} = m_{part}(1 - e^{-\psi})(v_{part} - v_{flow})\frac{1}{\Delta t}, \quad (A18)$$

where v_{part} and v_{flow} are velocities of the particle and the liquid flow, correspondingly. Hereby, the flow velocity is determined only in the X direction, and in the other axial directions it is equal to zero:

$$v_{flow,x} = \dot{\Gamma}|Z_{part}|, \quad (A19)$$

$$v_{flow,y} = v_{flow,z} = 0. \quad (A20)$$

Here, $\dot{\Gamma}$ is the shear rate and Z_{part} is the coordinate of the particles in Z direction.

The lift force F_{lift} is only defined in Z direction, whereas its X and Y components are equal to zero:

$$F_{lift,z} = 6.46\rho_{liq}\sqrt{\frac{\eta}{\rho_{liq}}}r_{part}^2\sqrt{|\dot{\Gamma}|}(v_{flow,x} - v_{part,x}), \quad (A21)$$

$$F_{lift,x} = F_{lift,y} = 0, \quad (A22)$$

where ρ_{liq} is density of the liquid.

Appendix A.2. Decanter Centrifuge

This section summarizes the most important geometric considerations regarding the decanter centrifuge model.

The compartment approach relies on the discretization of the unrolled screw within the cylindrical and conical part of the decanter centrifuge. The total length of the helix

$$L_{hel} = L_{cyl} + L_{con} \quad (A23)$$

is composed of the length of the cylindrical (L_{cyl}) and the conical (L_{con}) parts. The helix length of the cylindrical part depends on the number of screw turns N_{cyl} in the cylindrical part, the screw pitch B_k and the radius of the bowl R_b :

$$L_{cyl} = N_{cyl} \left((2\pi R_b)^2 + B_k^2 \right)^{0.5}. \quad (A24)$$

In the conical part of the centrifuge, the length of the unrolled screw is a function of the cone angle β . The Euclidean norm of the derivation of X to a variable position along the unrolled screw dl allows us to depict the length of the helix in the conical part:

$$L_{con} = \int_0^{2\pi N_{con}} \|\vec{X}'\| dl. \quad (A25)$$

The transition between the cylindrical-conical part at $l = 0$ and the solids discharge at $l = 2\pi N_{con}$ define the bounds of the integration. Thereby, N_{con} is the number of turns in the conical part. The Euclidean norm of the helix vector is

$$\begin{aligned} \|\vec{X}'\| = & \left(\left[-\frac{B_k}{2\pi} \tan \beta \cos l - \left(R_b - \frac{B_k}{2\pi} l \tan \beta \right) \sin \beta \right]^2 + \right. \\ & \left. + \left[-\frac{B_k}{2\pi} \tan \beta \sin l + \left(R_b - \frac{B_k}{2\pi} l \tan \beta \right) \cos \beta \right]^2 + \left[\frac{B_k}{2\pi} \right]^2 \right)^{0.5}. \end{aligned} \quad (A26)$$

Appendix A.3. Rotary Kiln

In this section, the constitutive equations for the kiln model are given. The overall properties of the phases are calculated by a weighted summation of the single compound properties.

Appendix A.3.1. Mass Flows

The outgoing mass flow rate of the solid phase is calculated as follows

$$\dot{m}_{out,s} = \dot{m}_{out,s}^{forw} - \dot{m}_{out,s}^{back} = v_s A_s \rho_s, \quad (A27)$$

with the axial velocity of the solids v_s , the cross-sectional area of the solids bed A_s and the solids density ρ_s . The information on v_s is extracted from coupled CFD-DEM simulations of the kiln and entered as a user-defined parameter.

The backwards directed mass flow rate is calculated by

$$\dot{m}_{out,s}^{back} = \frac{v_s \rho_s A_s}{Bo}, \quad (A28)$$

with the Bodenstein-number Bo , which is set as a user-defined parameter.

Since the fluid mechanics of the gas is not described in detail by the model, a simplified approach is taken to calculate the outgoing gas mass flow from a compartment. Therefore, a target mass of the gas is calculated according to the ideal gas law, and a control function is defined that ensures that the mass of the gas in the compartment is equal to the target mass:

$$\dot{m}_{g,out} = \frac{2m_g}{m_{target,g} + m_g} (\dot{m}_{in,g} + \sum_k^{N_k} \dot{m}_{g \leftrightarrow r,k}), \quad (A29)$$

with

$$m_{target,g} = \frac{p_g V_g M_g}{RT_g}. \quad (A30)$$

Appendix A.3.2. Reactions

The reaction mass flows for an exemplary reaction k are calculated as follows:

$$\dot{m}_{s/g \leftrightarrow r,k} = \sum_j^{N_C} \dot{m}_{s/g \rightarrow r,k,j} = \sum_j^{N_C} \frac{\nu_{s/g,k,j}}{\nu_{base,k}} r_k M_j, \quad (A31)$$

with the reaction rate r_k and the molar mass M . ν is the stoichiometric coefficient of the respective compound, where the index *base* indicates the base compound of this reaction.

The rate for reaction k is calculated by

$$r_k = S_p k_k \prod_j^{N_C} c_{s/g,j'}^{|v_j|} \quad (A32)$$

with the molecular concentration in the respective phase c and surface of the solid particles S_p . An Arrhenius approach is used for the calculation of the reaction constant k_k :

$$k_k = A_k \exp\left(\frac{-E_{A,k}}{RT_r}\right), \quad (A33)$$

where A_k is the reaction-specific rate constant, E_A is the reaction activation energy, R is the universal gas constant, and T_r is the reaction temperature.

For the considered reactions, the following constants are applied (Table A1).

Table A1. Stoichiometric coefficients for the combustion reaction and the evaporation of water from the solid bed.

Reaction	Base	$\nu_{s,C}$	ν_{s,H_2O}	ν_{g,O_2}	ν_{g,CO_2}	ν_{g,H_2O}
Calcination	C	-1	0	-1	1	0
Evaporation	H ₂ O ^(s)	0	-1	0	0	1

Appendix A.3.3. Heat Flows

The heat flow between the solid interface of the wall and the solid phase is calculated by

$$\dot{Q}_{ws \rightarrow s} = \alpha_{ws \rightarrow s} A_{ws} (T_{ws} - T_s). \quad (A34)$$

The convective heat transfer flows between exemplary phases p and q :

$$\dot{Q}_{p \rightarrow q} = \alpha_{p \rightarrow q} A_{pq} (T_p - T_q). \quad (A35)$$

The calculation of the different heat transfer coefficients is performed as shown below [36,53]:

$$\alpha_{ws \rightarrow s} = 11.6 \left(\frac{\omega r_i^2 f}{\alpha_s} \right)^{0.3} \frac{\lambda_{eff,s}}{\psi r_i}, \quad (A36)$$

$$\alpha_{s \rightarrow g} = 0.46 \frac{\lambda_g}{D_h} \text{Re}_{axi}^{0.535} \text{Re}_{ang}^{0.104} f^{-0.341}, \quad (A37)$$

$$\alpha_{wg \rightarrow g} = 1.54 \frac{\lambda_g}{D_h} \text{Re}_{axi}^{0.575} \text{Re}_{ang}^{-0.292}, \quad (A38)$$

with effective thermal conductivity $\lambda_{eff,s}$ depending on the bed porosity ξ :

$$\lambda_{eff,s} = \lambda_g \left(1 - \sqrt{1 - \xi} + \frac{2}{K_{\lambda,1}} \sqrt{1 - \xi} \cdot \left[\frac{1 - \frac{\lambda_g}{\lambda_s} K_{\lambda,2}}{K_{\lambda,1}^2 \ln \left(\frac{\lambda_s}{K_{\lambda,2} \lambda_g} - \frac{K_{\lambda,2} + 1}{2} - \frac{K_{\lambda,2} - 1}{K_{\lambda,1}} \right)} \right] \right), \quad (A39)$$

$$K_{\lambda,1} = 1 - \frac{\lambda_g}{\lambda_s} K_{\lambda,2}, \quad (A40)$$

$$K_{\lambda,2} = 1.25 \left(\frac{1 - \xi}{\xi} \right)^{\frac{10}{9}}, \quad (A41)$$

and

$$\text{Re}_{axi} = \frac{\rho_g D_h v_g}{\eta_g}, \quad (A42)$$

$$\text{Re}_{ang} = \frac{\rho_g D_h^2 \omega}{\eta_g}, \quad (A43)$$

$$D_h = 4 \frac{A_g}{A_{sg} + A_{ws}}, \quad (A44)$$

$$f = \frac{A_s}{\pi r_i^2}, \quad (A45)$$

$$v_g = \frac{0.5(\dot{m}_{in,g} + \dot{m}_{out,g})}{\rho_g A_g}, \quad (A46)$$

$$\alpha_s = \frac{\lambda_{eff,s}}{\rho_s c_{p,s}}. \quad (A47)$$

Here, λ is the thermal conductivity; ω is the kiln rotation velocity; α_s is the thermal diffusivity of the solid phase; c_p is the specific heat capacity; ψ is the central angle of

the solids bed; D_h is the hydraulic diameter; Re_{axi} and Re_{ang} are the axial and angular Reynold's numbers; f is the filling degree; η is the dynamic viscosity; r_i is the kiln inner radius.

The radiative heat transfer flows between exemplary phases p and q is calculated as

$$\dot{Q}_{p \rightarrow q, rad} = \epsilon_{p \rightarrow q} \sigma A_{pq} (T_p^4 - T_q^4), \quad (A48)$$

with the respective emissivities [54]

$$\epsilon_{s \rightarrow g} = \frac{\epsilon_s \epsilon_g \left(1 + \frac{A_{sg}}{A_{wg}} (1 - \epsilon_g)(1 - \epsilon_w) \right)}{1 - U}, \quad (A49)$$

$$\epsilon_{wg \rightarrow g} = \frac{\epsilon_w \epsilon_g \left(1 + \frac{A_{sg}}{A_{wg}} (1 - \epsilon_s)(1 - \epsilon_g) \right)}{1 - U}, \quad (A50)$$

$$\epsilon_{wg \rightarrow s} = \frac{\epsilon_s \epsilon_w (1 - \epsilon_g)}{1 - U}, \quad (A51)$$

where

$$U = (1 - \epsilon_g)(1 - \epsilon_w) \left[\frac{A_{sg}}{A_{wg}} (1 - \epsilon_s)(1 - \epsilon_g) + \left(1 - \frac{A_{sg}}{A_{wg}} \right) \right]. \quad (A52)$$

Here, σ is the Boltzmann constant.

The conductive heat flow rates between the wall and the wall-interfaces are calculated by

$$\dot{Q}_{w \rightarrow ws} = \frac{T_w - T_{ws}}{\ln\left(\frac{r_o + r_i}{2r_i}\right)} \psi \lambda_w L, \quad (A53)$$

$$\dot{Q}_{w \rightarrow wg} = \frac{T_w - T_{wg}}{\ln\left(\frac{r_o + r_i}{2r_i}\right)} (2\pi - \psi) \lambda_w L, \quad (A54)$$

where L is the compartment length and r_o is the outer radius of the kiln.

The regenerative heat flow is calculated by:

$$\dot{Q}_{ws \rightarrow wg} = \delta L \omega r_i \cdot \rho_w c_{p,w} \cdot (T_{ws} - T_{wg}), \quad (A55)$$

with a user-defined interface thickness δ .

Appendix A.3.4. Geometric Considerations

The cross-sectional area of the solid bed is calculated by

$$A_s = \frac{1}{1 - \xi} \frac{m_s}{\rho_s L}, \quad (A56)$$

with the bed porosity ξ .

The central angle of the solid bed ψ is calculated as

$$\psi = 2 \cos^{-1}(1 - 0.5H_s), \quad (A57)$$

where H_s is the solids bed height.

The surfaces through which heat transfer occurs are:

$$A_{sg} = 2r_i \sin\left(\frac{\psi}{2}\right) L, \quad (A58)$$

$$A_{ws} = r_i \psi L, \quad (A59)$$

$$A_{wg} = r_i (2\pi - \psi) L. \quad (A60)$$

Appendix A.4. Synthesis Simulation Parameters

Model parameters used to simulate synthesis unit in Section 3.1 are given in Table A2.

PSD was described with an equidistant volumetric grid with 1000 classes on the interval 0...1000 μm^3 .

Table A2. Model parameters of the Synthesis reactor used in Section 3.1.

Parameter		Value	Units
Initial holdup mass	m	5	kg
Initial fraction material M1	w_{M1}	0.077	kg kg^{-1}
Initial fraction material M2	w_{M2}	0	kg kg^{-1}
Initial fraction material M3	w_{M3}	0.208	kg kg^{-1}
Initial fraction material template	w_{Te}	0.05	kg kg^{-1}
Initial fraction water	w_{H_2O}	0.665	kg kg^{-1}
Temperature	T	440	K
Viscosity	η	0.0015	-
Surface energy	γ	0.1	$\text{J}^2 \text{m}^{-1}$
Shear rates	$\dot{\Gamma}$	6, 21, 60, 170, 290	s^{-1}
Shear rates fractions		0.01, 0.2, 0.4, 0.34, 0.05	-
Stoichiometric coefficient M1	ν_{M1}	1	-
Stoichiometric coefficient M2	ν_{M2}	2.33	-
Stoichiometric coefficient M3	ν_{M3}	34	-
Stoichiometric coefficient template	ν_{Te}	2	-
Reaction activation energy	E_A	1400	J mol^{-1}
Agglomeration rate constant	β_0	8×10^{-16}	-
Agglomeration rate constant Brownian	$\beta_{0,Br}$	1×10^{-5}	-
Agglomeration rate constant Shear	$\beta_{0,Sh}$	1×10^{14}	-
Nuclei diameter	D_{new}	0.08	μm
Pre-exponential factor for reaction 1	k_1	0.18	$(\text{mol}/\text{m}^3)^{1-n_{M1}}/\text{s}$
Pre-exponential factor for reaction 2	k_2	0.004	$(\text{mol}/\text{m}^3)^{1-n_{M2}-n_{M3}-n_{Te}}/\text{s}$
Model parameter	n_{M1}	0.44	-
Model parameter	n_{M2}	0.04	-
Model parameter	n_{M3}	0.045	-
Model parameter	n_{Te}	0.0001	-
Model parameter	$n_{Am,1}$	0.7	$(\text{mol}/\text{m}^3)^{1-n_{UC}}/\text{s}$
Model parameter	$n_{Am,2}$	0.65	$(\text{mol}/\text{m}^3)^{1-n_{UC}}/\text{s}$
Model parameter	n_{Cr}	0.33	-
Model parameter	n_{UC}	0.45	-
Model parameter	$k_{Am,1}$	1.01	-
Model parameter	$k_{Am,2}$	1.02	-
Model parameter	$k_{Cr,1}$	1×10^{-5}	s^{-1}
Model parameter	$k_{Cr,2}$	3×10^{-5}	s^{-1}
Model parameter	k_{uv1}	100	μm^3
Model parameter	k_{uv2}	1000	μm^3

Appendix A.5. Calcination Simulation Parameters

Model parameters used to simulate kiln unit in Section 3.2 are given in Table A3.

PSD was described with an equidistant grid with 10 classes on the interval 100...500 μm .

The combustion reaction was defined as:



Table A3. Model parameters of the Calciner unit used in Section 3.2.

Parameter		Value	Units
Initial solid holdup mass	m_s	100	kg
Initial solid holdup temperature	T_s	300	K
Initial solid holdup organic residue fraction	w_C	0.08	kg kg ⁻¹
Initial gas holdup mass	m_s	10	kg
Initial gas holdup temperature	T_s	300	K
Initial gas holdup oxygen fraction	w_{O_2}	0.23	kg kg ⁻¹
Solid inlet mass flow	$\dot{m}_{s,in}$	500	kg h ⁻¹
Solid inlet temperature	$T_{s,in}$	300	K
Solid inlet organic residue fraction	$w_{C,in}$	0.08	kg kg ⁻¹
Gas inlet mass flow	$\dot{m}_{s,in}$	450	kg h ⁻¹
Gas inlet temperature	$T_{s,in}$	300	K
Gas inlet oxygen fraction	$w_{O_2,in}$	0.23	kg kg ⁻¹
Number of compartments		20	-
Kiln length	L	10	m
Kiln diameter	D	1.5	m
Wall thickness		0.15	m
Rotation velocity	ω	2.5	rpm
Bed porosity	ζ	0.24	-
Solids velocity at solids inlet	$v_{s,beg}$	0.0025	m s ⁻¹
Solids velocity at solids outlet	$v_{s,end}$	0.005	m s ⁻¹
Combustion reaction rate constant	A_1	2.25×10^{-5}	m ⁴ s ⁻¹ mol ⁻³
Combustion reaction activation energy	$E_{A,1}$	99,970	J mol ⁻¹
Reaction layer		0.01	m
Reaction heat coefficient	K_H	0.5	-
Reaction temperature coefficient	K_T	0.5	-
Wall interface thickness	δ	0.05	m

Appendix A.6. Zeolite Production Simulation Parameters

Model parameters used to simulate the zeolite catalyst production process in Section 3.3 are given in Tables A4–A8.

Distributed parameters of particles were described as:

- Reactor, centrifuges: equidistant PSD grid with 1000 classes on the interval 0...20 μm.
- Spray dryer: equidistant PSD grid with 10 classes on the interval 20...300 μm, and equidistant grid for moisture content with 10 classes on the interval 0...1.
- Kiln: equidistant PSD grid with 10 classes on the interval 20...300 μm

Reactions in kilns were defined as:



Table A4. Model parameters of the Synthesis unit used in the flowsheet simulations of the zeolite catalyst production process.

Parameter		Value	Units
Initial holdup mass	m	2.484	kg
Initial fraction material M1	w_{M1}	0.077	kg kg ⁻¹
Initial fraction material M2	w_{M2}	0	kg kg ⁻¹
Initial fraction material M3	w_{M3}	0.208	kg kg ⁻¹
Initial fraction material template	w_{Te}	0.05	kg kg ⁻¹
Initial fraction water	w_{H_2O}	0.665	kg kg ⁻¹
Temperature	T	440	K
Viscosity	η	0.0015	-
Surface energy	γ	0.12	J ² m ⁻¹
Shear rates	$\dot{\Gamma}$	6, 7, 21, 60, 170, 290	s ⁻¹
Shear rates fractions		0.03, 0.3, 0.4, 0.2, 0.06, 0.01	-
Stoichiometric coefficient M1	ν_{M1}	1	-
Stoichiometric coefficient M2	ν_{M2}	2.33	-
Stoichiometric coefficient M3	ν_{M3}	34	-
Stoichiometric coefficient template	ν_{Te}	2	-
Reaction activation energy	E_A	1374	J mol ⁻¹
Agglomeration rate constant	β_0	1×10^{-12}	-
Agglomeration rate constant Brownian	$\beta_{0,Br}$	1×10^{-5}	-
Agglomeration rate constant Shear	$\beta_{0,Sh}$	1×10^{14}	-
Nuclei diameter	D_{new}	0.01	μm
Pre-exponential factor for reaction 1	k_1	0.187	(mol/m ³) ^{1-n_{M1}} /s
Pre-exponential factor for reaction 2	k_2	0.006	(mol/m ³) ^{1-n_{M2}-n_{M3}-n_{Te}} /s
Model parameter	n_{M1}	0.438	-
Model parameter	n_{M2}	0.017	-
Model parameter	n_{M3}	0.001	-
Model parameter	n_{Te}	0.023	-
Model parameter	$n_{Am,1}$	0.731	(mol/m ³) ^{1-n_{UC}} /s
Model parameter	$n_{Am,2}$	0.701	(mol/m ³) ^{1-n_{UC}} /s
Model parameter	n_{Cr}	0.325	-
Model parameter	n_{UC}	0.508	-
Model parameter	$k_{Am,1}$	1.006	-
Model parameter	$k_{Am,2}$	0.882	-
Model parameter	$k_{Cr,1}$	1.2×10^{-5}	s ⁻¹
Model parameter	$k_{Cr,2}$	4.103×10^{-5}	s ⁻¹
Model parameter	k_{uv1}	4.2	μm^3
Model parameter (Case 1)	k_{uv2}	245	μm^3
Model parameter (Case 2)	k_{uv2}	1440	μm^3

Table A5. Model parameters of the Centrifuge 1/Centrifuge 2 units used in the flowsheet simulations of the zeolite catalyst production process.

Parameter		Value	Units
Number of cylinder compartments		25	-
Number of cone compartments		25	-
Bowl radius	R_b	0.3/0.25	m
Weir radius	R_w	0.2115/0.13	m
Cylinder length	L_{cyl}	2.2/1	m
Cone length	L_{con}	0.5/0.3	m
Screw pitch	B_k	0.125/0.06	m
Cone angle	β	10	°
Bowl rotation speed	ω	3000/2200	rpm
Differential speed	Δn	5	rpm
Max filling		0.9	-

Table A5. *Cont.*

Parameter		Value	Units
Transport efficiency	k	0.25	-
Get point	ϕ_{gel}	0.08	$\text{m}^3 \text{m}^{-3}$
Hindrance coefficient 1	p_1	1.3	-
Hindrance coefficient 2	p_2	10	-
Hindrance coefficient 3	p_3	0	-
Maximum volume solid fraction	$\phi_{sed,max}$	0.77	$\text{m}^3 \text{m}^{-3}$

Table A6. Model parameters of the Washing water inlet used in the flowsheet simulations of the zeolite catalyst production process.

Parameter	Value	Units
Mass flow	7200	kg h^{-1}
Temperature	293.7	K

Table A7. Model parameters of the Spray dryer unit used in the flowsheet simulations of the zeolite catalyst production process.

Parameter		Value	Units
Residence time	τ_p	2	s
Relative velocity	τ_{rel}	0.01	m s^{-1}
Number of height compartments	n_{el}	400	
Critical moisture content	X_{cr}	0.7	kg kg^{-1}
Equilibrium moisture content	X_{eq}	0.01	kg kg^{-1}
Spray dryer height	H	8	m
Height of cylindrical part	H_{cyl}	5	m
Diameter of cylindrical part	D_{cyl}	4	m
Diameter of outlet	D_{out}	0.2	m
Ambient temperature	T_{amb}	293.15	K
Wall heat conductivity	λ_W	50	$\text{W m}^{-1} \text{K}^{-1}$
Wall thickness	t_W	0.2	m
Inlet gas mass flow		10,800	kg h^{-1}
Inlet gas temperature		623	K

Table A8. Model parameters of the Calciner 1/Calciner 2 units used in the flowsheet simulations of the zeolite catalyst production process.

Parameter		Value	Units
Initial solid holdup mass	m_s	20	kg
Initial solid holdup temperature	T_s	300	K
Initial solid holdup organic residue fraction	w_C	0.1	kg kg^{-1}
Initial gas holdup mass	m_s	10	kg
Initial gas holdup temperature	T_s	300	K
Initial gas holdup oxygen fraction	w_{O_2}	0.23	kg kg^{-1}
Gas inlet mass flow	$\dot{m}_{s,in}$	450	kg h^{-1}
Gas inlet temperature	$T_{s,in}$	300	K
Gas inlet oxygen fraction	$w_{O_2,in}$	0.05/0.23	kg kg^{-1}
Number of compartments		10	-
Kiln length	L	12	m
Kiln diameter	D	1.5	m
Wall thickness		0.15	m

Table A8. Cont.

Parameter		Value	Units
Rotation velocity	ω	2.5	rpm
Bed porosity	ζ	0.24	-
Solids velocity at solids inlet	$v_{s,beg}$	0.0025	m s^{-1}
Solids velocity at solids outlet	$v_{s,end}$	0.005	m s^{-1}
Wall temperature	T_w	973	K
Bodenstein number	Bo	1×10^{10}	-
Combustion reaction rate constant	A_1	2.25×10^{-5}	$\text{m}^4 \text{s}^{-1} \text{mol}^{-3}$
Combustion reaction activation energy	$E_{A,1}$	99970	J mol^{-1}
Evaporation reaction rate constant	A_2	0.00015	$\text{m}^4 \text{s}^{-1} \text{mol}^{-3}$
Evaporation reaction activation energy	$E_{A,2}$	43800	J mol^{-1}
Reaction layer		0.01	m
Reaction heat coefficient	K_H	0.5	-
Reaction temperature coefficient	K_T	0.5	-
Wall interface thickness	δ	0.05	m

References

- Ennaert, T.; van Aelst, J.; Dijkmans, J.; de Clercq, R.; Schutyser, W.; Dusselier, M.; Verboekend, D.; Sels, B.F. Potential and challenges of zeolite chemistry in the catalytic conversion of biomass. *Chem. Soc. Rev.* **2016**, *45*, 584–611. [\[CrossRef\]](#)
- Alonso, A.; Moral-Vico, J.; Abo Markeb, A.; Busquets-Fité, M.; Komilis, D.; Puentes, V.; Sánchez, A.; Font, X. Critical review of existing nanomaterial adsorbents to capture carbon dioxide and methane. *Sci. Total. Environ.* **2017**, *595*, 51–62. [\[CrossRef\]](#)
- Lin, C.C.H.; Dambrowitz, K.A.; Kuznicki, S.M. Evolving applications of zeolite molecular sieves. *Can. J. Chem. Eng.* **2012**, *90*, 207–216. [\[CrossRef\]](#)
- Feliczak-Guzik, A. Hierarchical zeolites: Synthesis and catalytic properties. *Microporous Mesoporous Mater.* **2018**, *259*, 33–45. [\[CrossRef\]](#)
- Mardiana, S.; Azhari, N.J.; Ilmi, T.; Kadja, G.T. Hierarchical zeolite for biomass conversion to biofuel: A review. *Fuel* **2022**, *309*, 122119. [\[CrossRef\]](#)
- Smit, B.; Maesen, T.L.M. Molecular simulations of zeolites: Adsorption, diffusion, and shape selectivity. *Chem. Rev.* **2008**, *108*, 4125–4184. [\[CrossRef\]](#)
- Abdelrasoul, A.; Zhang, H.; Cheng, C.H.; Doan, H. Applications of molecular simulations for separation and adsorption in zeolites. *Microporous Mesoporous Mater.* **2017**, *242*, 294–348. [\[CrossRef\]](#)
- Mollahosseini, A.; Abdelrasoul, A. Molecular dynamics simulation for membrane separation and porous materials: A current state of art review. *J. Mol. Graph. Model.* **2021**, *107*, 107947. [\[CrossRef\]](#)
- Schwalbe-Koda, D.; Kwon, S.; Paris, C.; Bello-Jurado, E.; Jensen, Z.; Olivetti, E.; Willhammar, T.; Corma, A.; Román-Leshkov, Y.; Moliner, M.; et al. A priori control of zeolite phase competition and intergrowth with high-throughput simulations. *Science* **2021**, *374*, 308–315. [\[CrossRef\]](#)
- Jelfs, K.E.; Slater, B.; Lewis, D.W.; Willock, D.J. The role of organic templates in controlling zeolite crystal morphology. In *From Zeolites to Porous MOF Materials-The 40th Anniversary of International Zeolite Conference, Proceedings of the 15th International Zeolite Conference, Beijing, China, 12–17 August 2007*; Studies in Surface Science and Catalysis; Elsevier: Amsterdam, The Netherlands, 2007; Volume 170, pp. 1685–1692. [\[CrossRef\]](#)
- Ma, S.; Liu, Z.P. The Role of Zeolite Framework in Zeolite Stability and Catalysis from Recent Atomic Simulation. *Top. Catal.* **2022**, *65*, 59–68. [\[CrossRef\]](#)
- Ma, S.; Liu, Z.P. Machine learning potential era of zeolite simulation. *Chem. Sci.* **2022**, *13*, 5055–5068. [\[CrossRef\]](#) [\[PubMed\]](#)
- Jeffroy, M.; Boutin, A.; Fuchs, A.H. Understanding the equilibrium ion exchange properties in faujasite zeolite from Monte Carlo simulations. *J. Phys. Chem. B* **2011**, *115*, 15059–15066. [\[CrossRef\]](#) [\[PubMed\]](#)
- Pophale, R.; Cheeseman, P.A.; Deem, M.W. A database of new zeolite-like materials. *Phys. Chem. Chem. Phys. PCCP* **2011**, *13*, 12407–12412. [\[CrossRef\]](#) [\[PubMed\]](#)
- Dai, H.; Shen, Y.; Yang, T.; Lee, C.; Fu, D.; Agarwal, A.; Le, T.T.; Tsapatsis, M.; Palmer, J.C.; Weckhuysen, B.M.; et al. Finned zeolite catalysts. *Nat. Mater.* **2020**, *19*, 1074–1080. [\[CrossRef\]](#)
- Jiang, N.; Erdős, M.; Moulτος, O.A.; Shang, R.; Vlugt, T.J.; Heijman, S.G.; Rietveld, L.C. The adsorption mechanisms of organic micropollutants on high-silica zeolites causing S-shaped adsorption isotherms: An experimental and Monte Carlo simulation study. *Chem. Eng. J.* **2020**, *389*, 123968. [\[CrossRef\]](#)
- Sherwood, P.; de Vries, A.H.; Collins, S.J.; Greatbanks, S.P.; Burton, N.A.; Vincent, M.A.; Hillier, I.H. Computer simulation of zeolite structure and reactivity using embedded cluster methods. *Faraday Discuss.* **1997**, *106*, 79–92. [\[CrossRef\]](#)
- van Erp, T.S.; Caremans, T.P.; Kirschhock, C.E.A.; Martens, J.A. Prospects of transition interface sampling simulations for the theoretical study of zeolite synthesis. *Phys. Chem. Chem. Phys. PCCP* **2007**, *9*, 1044–1051. [\[CrossRef\]](#)
- Jackson, R.A.; Catlow, C.R.A. Computer Simulation Studies of Zeolite Structure. *Mol. Simul.* **1988**, *1*, 207–224. [\[CrossRef\]](#)

20. Ren, N.; Bronić, J.; Jelić, T.A.; Palčić, A.; Subotić, B. Seed-Induced, Structure Directing Agent-Free Crystallization of Sub-Micrometer Zeolite ZSM-5: A Population Balance Analysis. *Cryst. Growth Des.* **2012**, *12*, 1736–1745. [[CrossRef](#)]
21. Bosnar, S.; Antonić-Jelić, T.; Bronić, J.; Krznarić, I.; Subotić, B. Influence of anions on the kinetics of zeolite A crystallization. *J. Cryst. Growth* **2004**, *267*, 270–282. [[CrossRef](#)]
22. Thompson, R.W.; Dyer, A. A modified population balance model for hydrothermal molecular sieve zeolite synthesis. *Zeolites* **1985**, *5*, 292–301. [[CrossRef](#)]
23. Sheikh, A.Y.; Jones, A.G.; Graham, P. Population balance modeling of particle formation during the chemical synthesis of zeolite crystals: Assessment of hydrothermal precipitation kinetics. *Zeolites* **1996**, *16*, 164–172. [[CrossRef](#)]
24. Wang, L.G.; Ge, R.; Chen, X.; Zhou, R.; Chen, H.M. Multiscale digital twin for particle breakage in milling: From nanoindentation to population balance model. *Powder Technol.* **2021**, *386*, 247–261. [[CrossRef](#)]
25. Gandhi, A.; Hasan, M.M.F. Machine learning for the design and discovery of zeolites and porous crystalline materials. *Curr. Opin. Chem. Eng.* **2022**, *35*, 100739. [[CrossRef](#)]
26. Moliner, M.; Román-Leshkov, Y.; Corma, A. Machine Learning Applied to Zeolite Synthesis: The Missing Link for Realizing High-Throughput Discovery. *Accounts Chem. Res.* **2019**, *52*, 2971–2980. [[CrossRef](#)] [[PubMed](#)]
27. Farag, I.; Zhang, J. Simulation of Synthetic Zeolites-S4A and 5A Manufacturing for Green Processing. *Eng. Sci. Technol. Int. J.* **2012**, *2*, 188–195.
28. Salam, K.K.; Oke, E.O.; Ude, C.J.; Yahaya, U. Zeolite-Y-based catalyst synthesis from Nigerian Elefun Metakaolin: Computer-aided batch simulation, comparative predictive response surface and neuro-fuzzy modelling with optimization. *Chem. Pap.* **2022**, *76*, 1213–1224. [[CrossRef](#)]
29. Cundy, C.S.; Cox, P.A. The hydrothermal synthesis of zeolites: Precursors, intermediates and reaction mechanism. *Microporous Mesoporous Mater.* **2005**, *82*, 1–78. [[CrossRef](#)]
30. Barrasso, D.; Tamrakar, A.; Ramachandran, R. A reduced order PBM–ANN model of a multi-scale PBM–DEM description of a wet granulation process. *Chem. Eng. Sci.* **2014**, *119*, 319–329. [[CrossRef](#)]
31. Dosta, M.; Chan, T.T. Linking process-property relationships for multicomponent agglomerates using DEM-ANN-PBM coupling. *Powder Technol.* **2022**, *398*, 117156. [[CrossRef](#)]
32. Gleiss, M.; Nirschl, H. Modeling Separation Processes in Decanter Centrifuges by Considering the Sediment Build-Up. *Chem. Eng. Technol.* **2015**, *38*, 1873–1882. [[CrossRef](#)]
33. Gleiss, M.; Hammerich, S.; Kespe, M.; Nirschl, H. Application of the dynamic flow sheet simulation concept to the solid–liquid separation: Separation of stabilized slurries in continuous centrifuges. *Chem. Eng. Sci.* **2017**, *163*, 167–178. [[CrossRef](#)]
34. Gleiß, M. Dynamische Simulation der Mechanischen Flüssigkeitsabtrennung in Vollmantelzentrifugen. Ph.D Thesis, KIT Scientific Publishing, Karlsruhe, Germany, 2018. [[CrossRef](#)]
35. Buchholz, M.; Haus, J.; Pietsch-Braune, S.; Kleine Jäger, F.; Heinrich, S. CFD-aided population balance modeling of a spray drying process. *Adv. Powder Technol.* **2022**, *33*, 103636. [[CrossRef](#)]
36. Küssel, U. *Objektorientierte Modellbildung und Modellprädiktive Regelung von Drehrohröfen*. Ph.D. Thesis, VDI-Verl., Düsseldorf, Germany, 2011; Volume 1192.
37. Skorych, V.; Dosta, M.; Hartge, E.U.; Heinrich, S. Novel system for dynamic flowsheet simulation of solids processes. *Powder Technol.* **2017**, *314*, 665–679. [[CrossRef](#)]
38. Skorych, V.; Dosta, M.; Heinrich, S. Dyssol—An open-source flowsheet simulation framework for particulate materials. *SoftwareX* **2020**, *12*, 100572. [[CrossRef](#)]
39. Skorych, V.; Buchholz, M.; Dosta, M.; Heinrich, S. A Framework for Dynamic Simulation of Interconnected Solids Processes. In *Dynamic Flowsheet Simulation of Solids Processes*; Heinrich, S., Ed.; Springer International Publishing: Cham, Switzerland, 2020; pp. 581–628. [[CrossRef](#)]
40. Johnson, K.L.; Kendall, K.; Roberts, A.D. Surface energy and the contact of elastic solids. *Proc. R. Soc. Lond. A Math. Phys. Sci.* **1971**, *324*, 301–313. [[CrossRef](#)]
41. Depta, P.N.; Jandt, U.; Dosta, M.; Zeng, A.P.; Heinrich, S. Toward Multiscale Modeling of Proteins and Bioagglomerates: An Orientation-Sensitive Diffusion Model for the Integration of Molecular Dynamics and the Discrete Element Method. *J. Chem. Inf. Model.* **2019**, *59*, 386–398. [[CrossRef](#)]
42. Mościński, J.; Bargieł, M.; Rycerz, Z.A.; Jacobs, P.W.M. The Force-Biased Algorithm for the Irregular Close Packing of Equal Hard Spheres. *Mol. Simul.* **1989**, *3*, 201–212. [[CrossRef](#)]
43. Otsubo, M.; O’Sullivan, C.; Shire, T. Empirical assessment of the critical time increment in explicit particulate discrete element method simulations. *Comput. Geotech.* **2017**, *86*, 67–79. [[CrossRef](#)]
44. Dosta, M.; Skorych, V. MUSEN: An open-source framework for GPU-accelerated DEM simulations. *SoftwareX* **2020**, *12*, 100618. [[CrossRef](#)]
45. TensorFlow. An End-To-End Open Source Machine Learning Platform. Available online: <https://www.tensorflow.org> (accessed on 18 October 2022).
46. Keras: The Python Deep Learning API. Available online: <https://keras.io> (accessed on 18 October 2022).
47. Kingma, D.P.; Ba, J. Adam: A Method for Stochastic Optimization. In Proceedings of the 3rd International Conference on Learning Representations, San Diego, CA, USA, 7–9 May 2015.
48. Keras2cpp library. Available online: <https://github.com/gosha20777/keras2cpp> (accessed on 18 October 2022).

49. Kumar, S.; Ramkrishna, D. On the solution of population balance equations by discretization—I. A fixed pivot technique. *Chem. Eng. Sci.* **1996**, *51*, 1311–1332. [[CrossRef](#)]
50. Menesklou, P.; Nirschl, H.; Gleiss, M. Dewatering of finely dispersed calcium carbonate-water slurries in decanter centrifuges: About modelling of a dynamic simulation tool. *Sep. Purif. Technol.* **2020**, *251*, 117287. [[CrossRef](#)]
51. Martins, M.A.; Oliveira, L.S.; Franca, A.S. Modelling and simulation of limestone calcination in rotary kilns, Part 1: Pilot kiln. *ZKG Int.* **2002**, *55*, 76–87.
52. Ginsberg, T.; Modigell, M. Dynamic modelling of a rotary kiln for calcination of titanium dioxide white pigment. *Comput. Chem. Eng.* **2011**, *35*, 2437–2446. [[CrossRef](#)]
53. Tscheng, S.H.; Watkinson, A.P. Convective heat transfer in a rotary kiln. *Can. J. Chem. Eng.* **1979**, *57*, 433–443. [[CrossRef](#)]
54. Ginsberg, T. Dynamische Modellierung von Drehrohröfen. Ph.D. Thesis, Hochschulbibliothek der Rheinisch-Westfälischen Technischen Hochschule Aachen, Aachen, Germany, 2011.